An Interface-enriched Level Set Topology Optimization for designing mandibular reconstruction plates made from a functionally graded material

Jeffrey van der Zeeuw

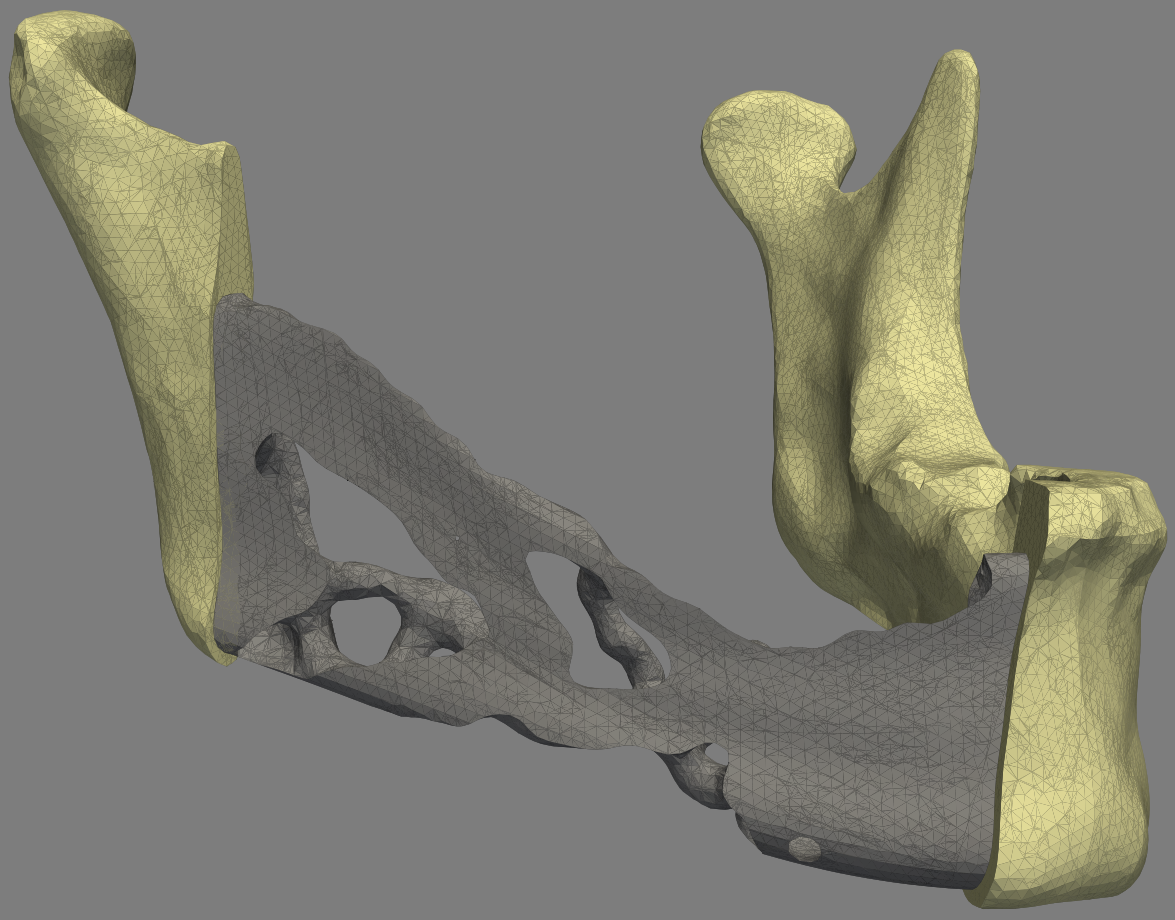

TU Delft

An Interface-enriched Level Set Topology Optimization for designing mandibular reconstruction plates made from a functionally graded material

Jeffrey van der Zeeuw

to obtain the degree of Master of Science
at the Delft University of Technology,
to be defended publicly on Monday September 23, 2024 at 8:45 AM.

Student Number:	4457072
Project Duration:	February, 2022 - September, 2024
Faculty:	Faculty of Mechanical Engineering, Delft
Thesis committee:	Dr. A. M Aragón, chair & supervisor
	Prof. Dr. J. Dankelman
	Dr. S van den Boom

TU Delft

Abstract

Increased capabilities of additive manufacturing technologies have opened up numerous possibilities in mandibular reconstruction surgery. For example, 3D scans can be used to design patient-specific reconstruction plates, resulting in designs that are tailored to prevent plate fracture, wound dehiscence, and malocclusion. However, screw loosening as a result of stress shielding is still an issue. This phenomenon is caused by the mismatch in stiffness between the bone and implant material. The stiffness of the titanium in these reconstruction plates can be reduced by using porous microstructures in the proximity of the remaining mandible. However, this makes intuition-based design impossible. This work applies computational tools to optimize the design of a mandibular reconstruction plate with varying microstructure porosity. To achieve this, Topology Optimization (TO) is used that accurately resolves boundaries utilizing the Interface-enriched Generalized Finite Element Method (IGFEM), which results in a smooth representation of the design. In this work, this methodology is enhanced to result in an even smoother and more accurate boundary. Moreover, additions are made to account for varying material properties in the analytical sensitivities of the compliance objective. The functionally graded designs exhibit significantly higher compliance that should reduce stress shielding. Also, they feature a more porous microstructure near the bone, providing a basis for bone ingrowth. Thus, it is established that enriched TO can be used to optimize the design of mandibular reconstruction plates made out of functionally graded materials that could reduce the risk of screw loosening.

Keywords— enriched finite element methods, topology optimization, level sets, functionally graded materials, mandibular reconstruction

Contents

1

Introduction

Oral and oropharyngeal cancer occurs in more than 450,000 cases worldwide [114] and the subsequent resection surgery has a far-reaching influence on the lives of patients, both physically and mentally. Physically, because it can lead to impaired masticatory function [42], which in turn could have a detrimental effect on the digestive system [83, 84]. Also mentally, because this condition and the subsequent surgery often alter the facial contour, making it less symmetric. This side effect can lead to increased stress and anxiety levels and reduced self-confidence [108, 79]. Some patients even consider becoming a normal member of society again even more important than successful resection of the tumour and the possibility of recurrences [66].

During the Second World War much experience was gained on mandibular reconstruction. For example, the application of bone grafts originating from different bones in the body, like ribs, the fibula or the ilium [9] was first proposed in this period. In 1989 the first work was submitted on sourcing a part of the fibula with surrounding soft tissue to bridge a defect in the mandible, calling it a free flap instead of a bone graft [44]. This would later become the “golden standard” in mandibular reconstruction [117, 29]. Using the fibular bone is desirable because of the amount of available material and its quality. Also, both the vascularization in the surrounding soft tissue and the nearby peroneal artery can provide nutrients to help osseointegration [37]. These favourable conditions all lead to a high success rate, which in this case means there is no loss of the graft material. This success rate has been reported to be up to $95\,\%$ [20, 60, 107, 18]. However, this type of surgery is not always possible because of the health of the patient [80]. Donor site morbidity and subsequent pain during walking have also been reported [4, 37, 61]. Furthermore, the slender form of the fibula means there is a discrepancy in the shape as compared to the intact mandible. This makes the placement of dental implants more complex [3], in some cases even requiring “double-barreling”, where two parts of the fibula are stacked on top of each other [62].

If, because of the reasons above, a reconstruction with tissue from the patient is not possible, titanium Arbeitsgemeinschaft für Osteosynthesefragen (AO) mandibular reconstruction plates or Titanium Hollow Osseointegrating Reconstruction Plates (THORP) are an established alternative that have been used since the 1980’s [61]. These slender plates bridge the defect in the mandible and offer multiple holes for rigid fixation to the mandible using screws. The type of screws represents the main difference between these two, with the THORP system using perforated hollow screws in combination with an expansion bolt in the screw head. In contrast, the AO system uses conventional titanium screws. The hollow screw heads allow bone to grow into them, resulting in a more rigid fixation and not requiring the Reconstruction Plate (RP) to be pressed against the bone, which can lead to pressure-induced bone necrosis [123]. Both systems are one-size-fits-all solutions. This not only makes them reasonably affordable, but it also allows for stock-keeping, which results in less time required before an operation. However, because these plates are not specifically manufactured to fit the patient, they need to be bent during the operation by a surgeon to fit the remaining bone and to preserve the preoperative facial contour. This bending results in residual stresses [78, 105], which combined with the fixation holes in the plate that cause stress concentrations [56, 80], can lead to failure of the plate by means of fracture. This type of mechanical failure occurs in $3.6\,\%$ to $10.7\,\%$ of patients [56, 53, 105, 103]. Other modes of failure of an RP are screw loosening and wound dehiscence and infection, while asymmetry, malocclusion and heat sensitivity have been reported as other complications after this type of mandibular reconstruction surgery [90]. This is reflected by failure rates of RPs, which have been reported to be anywhere in the range from $7\,\%$ to $37\,\%$ [53, 79, 105, 51].

With increased capabilities in the field of small-scale manufacturing of parts made from biocompatible materials, such as Selective Laser Melting (SLM) 3D printers that can use titanium alloys, possibilities have opened for research on patient-specific solutions [81, 68, 63]. These custom-made parts improve on the conventional RPs in cases where fibular free flap surgery is not an option. They can be designed to fit the shape of a 3D scan of the patient's remaining mandible and manufactured before the surgery. Because of this, no bending is required during the operation, reducing both operation time and failure rate of the RP by means of plate fracture [130]. This reduced failure rate is due to the design only having holes at the required screw locations and fewer features that cause stress concentrations. It also allows under-contouring of the design near locations with risk of wound dehiscence [80] and a patient-specific fit that minimizes the risk of asymmetry and malocclusion. However, the issue of screw loosening is still unsolved.

The key to solving the remaining issue of screw loosening is to analyze the stresses and strains acting in the RP and the surrounding bone during typical mastication tasks. This is possible by means of Finite Element Analysis (FEA) on a discretized model of the plate and the mandible, allowing the designer to predict the behaviour of a design [80, 86, 85]. By using FEA, it was found that the introduction of a titanium RP significantly alters the stress distribution in the mandible [94, 82]. In this changed situation, stresses are concentrated around the RP's fixation screws, removing local mechanical stimuli from other regions in the mandible [39]. This phenomenon is called stress shielding [75, 113, 49, 86] and leads to increased bone porosity and resorption [119], which causes screw loosening [32, 78]. Stress shielding is caused by a mismatch between bone and implant material [17, 21]. This mismatch indeed occurs for mandibular RPs, as biocompatible titanium's Young's modulus is $116\,\mathrm{GPa}$ [73, 36]. This is more than eight times that of cortical bone, which has a Young's modulus of $13.7\,\mathrm{GPa}$. The discrepancy is even larger when comparing it with cancellous bone at $0.4\,\mathrm{GPa}$ [93]. This means there is a risk of stress shielding and subsequent screw loosening in RPs, supported by accompanying failure rates ranging from $4.3\,\%$ to $5\,\%$ accounted to screw loosening for conventional RPs [53, 79]. Failure rates of patient-specific plates due to screw loosening have not been sufficiently studied.

A solution to this stress shielding problem can be found in nature, where a jump in stiffness occurs, for example in the attachment of muscles to bone. The tendons that connect the two create a smooth transition in stiffness. This happens by means of the microstructure of the tendon, where the shape and alignment of the collagen fibres gradually change, influencing its stiffness [118, 96]. This variation is combined with the shape of the tendon, widening at the connection point to the bone to maximize contact area yields optimal distribution of muscle forces to the bone. Also, inspiration can be drawn from the structure of bone itself. During bending and torsion loads, the outer shell of the bone experiences the majority of typical loads. This shell consists of the stiffer cortical bone while the middle consists of the porous cancellous bone with lower stiffness and weight. This spatial variation of the microstructure results in optimal stiffness while minimizing mass [41].

Designs similar to those found in nature have been proposed and used in the design of RPs for multiple bones in the body. Various microstructures have been proposed to reduce the effective stiffness of implant material used in bone reconstruction [124, 15, 45]. Also, a variable microstructure was used in a hip head replacement [58] to distribute stresses along the bone-implant interface more evenly. The reduction of stiffness of the material is not the only advantage that a porous microstructure brings, it also is more permeable to nutrients that are crucial for bone regrowth [50, 8]. It can also aid osseointegration, where newly generated bone grows into the voids of the structure, thus further improving the stability of the plate and load transfer during recovery [55, 129].

However, the balance that this functionally graded design needs to strike is very fine, as it needs to withstand typical loads while being flexible enough to prevent stress shielding [47, 67]. The complexity of this problem makes it impossible to design a functionally graded RP purely on intuition. An alternative is to apply computational design tools such as Topology Optimization (TO) to survey the design space. TO has been used to design mandibular RPs to ensure mechanical stability [73, 68]. Research has been done on using TO structures with varying microstructures [132, 112], showing it can be used to obtain an optimal distribution of material for such a problem. However, to the best of our knowledge, TO has not been used to design functionally graded mandibular RPs to reduce stress shielding. Using this approach could result in a design that not only can sustain the forces during mastication, but also prevent wound dehiscence, asymmetry and stress shielding that lead to screw loosening, thus inhibiting the most prevalent modes of plate failure.

The goal of this work is to apply TO to design a RP that bridges a mandibular defect, using a functionally graded material. To achieve this, TO based on the Interface-enriched Generalized Finite Element Method (IGFEM) is used. This method uses local subdivision of elements and an enriched definition of the Finite Element Method to yield a smooth description of the material boundary [109]. It has been used for compliance minimization [12], but also for fields where a smooth boundary representation is crucial, such as bandgap maximization in phononic crystals [13], designing nanophotonic devices [7], and for tailoring fracture resistance in brittle materials [131].

This work builds on that of van den Boom et al.[12] and uses the same FEA, objective function, and geometry description. To enhance the framework, we introduce a quadratic approximation for the boundary location along

element edges. This, in combination with regularization by means of periodic reinitialization of the level set function, results in an even smoother boundary representation. Since these improvements focus on the representation of the boundary, they can be implemented on any type of enriched TO. Also, a functionally graded material is introduced that represents variations in microstructure porosity and geometry. Such a material results in a more compliant RP with the material being distributed towards the remaining bone. The resulting design provides nearby bone with a porous basis that promotes bone ingrowth.

2

Work

2.1. Improving on IGFEM level set-based TO

2.1.1. Representation of a design by the level set function

In TO, there are different ways in which to connect the design variables to the actual design that one tries to optimize. In density-based TO, the design variables are, as the name suggests, related to a density field. This density field determines whether an element is part of the design domain or not, like for example with the Solid Isotropic Material with Penalization (SIMP) method [6]. However, in this work the design is represented by a Level Set Function (LSF) $\phi(\boldsymbol{x})$ [104, 121]. This function varies through the design domain and can be both positive and negative, dividing the design domain Ω as follows:

$$\begin{cases} \phi(\boldsymbol{x}) = 0, \text{ if } \boldsymbol{x} \in \Gamma_m \,, \\ \phi(\boldsymbol{x}) < 0, \text{ if } \boldsymbol{x} \in \Omega_s \,, \\ \phi(\boldsymbol{x}) > 0, \text{ if } \boldsymbol{x} \in \Omega_v \,. \end{cases} \tag{2.1}$$

The zero contour represents a material boundary Γ_m, where the material domain Ω_s is in contact with the void domain Ω_v. This allocation into different domains is visualized in Figure 2.1. At the start of every design iteration of the optimization, the value of the LSF at each node in the mesh is stored in a vector $\boldsymbol{\phi}$. After the initialization of these nodal level set values, every element edge is analyzed to check for a sign change in the LSF. If this is indeed the case, the element edge and thus the element is crossed by Γ_m.

It is possible to represent the design directly via nodal level set values $\boldsymbol{\phi}$ and interpolate the LSF between these nodes. However, an alternative is to place design variables more sparsely across the design domain and construct the LSF as a superposition of basis functions [100], for example, Radial Basis Functions (RBFs) [65, 24]. In this work, a compactly supported RBF is used [122]. How this function spreads the influence of design variables can also be seen in Figure 2.1. The equation for the compactly supported RBF is defined as

$$\theta_i(r_i) = (1 - r_i)^4 (4r_i + 1) \,, \tag{2.2}$$

where the radius r_i is the normalized Euclidian distance between the location at which the function is analyzed and the base of the RBF $\boldsymbol{x}_i$:

$$r_i(\boldsymbol{x}, \boldsymbol{x}_i) = \frac{\sqrt{\|\boldsymbol{x} - \boldsymbol{x}_i\|}}{r_s} \,, \tag{2.3}$$

and r_s is the radius of the support. Equation (2.2) shows some desirable behaviour, as its output ranges between 0 and 1 by definition and its region of influence can be adjusted as desired. By increasing the region of influence, one design variable influences a larger part of the design domain. This can allow for the optimizer to take larger steps, which leads to quicker convergence of the optimization [12]. The RBFs also give control over the complexity of designs [12]. Moreover, this method decouples the mesh from the design variables. This means that a finer discretization can be used if desired, resulting in a reduced design space. With these definitions, the value of the

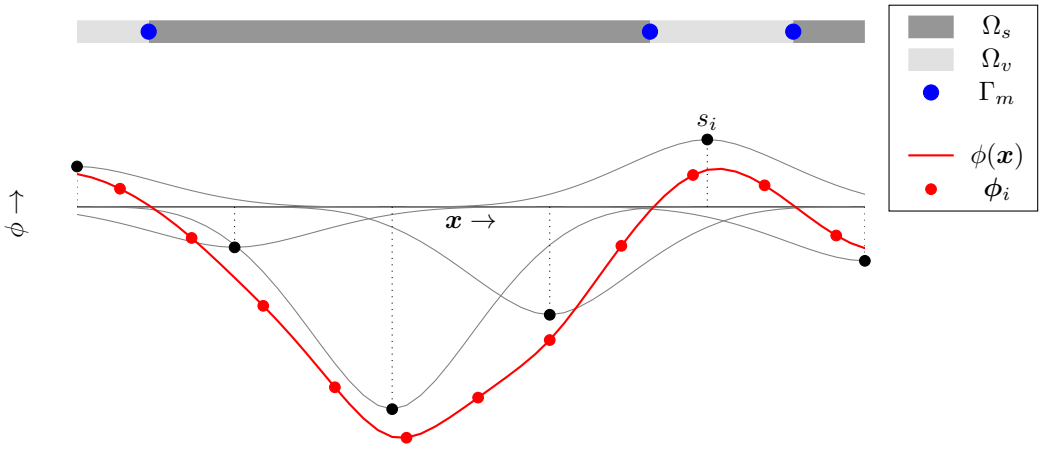

Figure 2.1: One-dimensional representation of the design domain Ω, decomposed into Ω_s, Ω_v and Γ_m by means of the LSF, as described in Equation (2.1). In this figure, the black lines are the RBFs that span the influence of design variables s_i. The LSF is represented by the solid red line. However, during most computational procedures only the nodal level set values $\boldsymbol{\phi}_i$ are known, as depicted by the red dots.

LSF at any location $\boldsymbol{x}$ in the design domain can be found by adding the contribution of every design variable whose corresponding RBF is nonzero at $\boldsymbol{x}$, represented by index set ι_s:

$$\phi(\boldsymbol{x}) = \sum_{i \in \iota_s} \theta_i(\boldsymbol{x}) s_i \,. \tag{2.4}$$

To reduce computational cost during the optimization, the contribution of each RBF on every mesh node in the analysis can be calculated in advance and stored in a matrix $\boldsymbol{\theta}$. This calculation needs to be carried out only once, after which the level set values can be found using the simple matrix multiplication:

$$\boldsymbol{\phi} = \boldsymbol{\theta}^\intercal \boldsymbol{s} \,, \tag{2.5}$$

where $\boldsymbol{s}$ is a vector with all the design variables. Note that the calculation of the contributions of each RBF in advance is only possible if there is no remeshing done during the optimization. Remeshing can move and add mesh nodes and hereby change the influence that nodes encounter from each RBF in matrix $\boldsymbol{\theta}$. This circumvention of remeshing is possible by using the Interface-enriched General Finite Element Method (IGFEM) to solve the finite element problem, which is discussed in more detail in Section 2.1.2.

Note the smoothing behaviour of the RBFs in Figure 2.1. Also note that equation (2.5) clearly shows the decoupling of the nodal level set values of the mesh with respect to the design variables. For any set of design variables $\boldsymbol{s}$ combined with RBFs with a radius r_s, any mesh can be used to discretize this design. To do this, the matrix $\boldsymbol{\theta}^\intercal$ needs to be calculated to connect $\boldsymbol{s}$ and $\boldsymbol{\phi}$ for this combination of mesh and RBFs. This means that a finer mesh can lead to a more accurate approximation of Γ_m, like increasing the number of nodal level set values $\boldsymbol{\phi}_i$ in Figure 2.1. This interaction can be done while keeping the same number of design variables and only requires the recalculation of $\boldsymbol{\theta}$.

2.1.2. The Interface-enriched Generalized Finite Element Method

Now that the design can be represented, an elastostatics problem such as the one described in the schematic in Figure 2.2 needs to be solved to find displacements, stresses $\boldsymbol{\sigma}$ and strains $\boldsymbol{\epsilon}$ in the material. The weak form of such a problem can be written as

$$\mathcal{B}(\boldsymbol{u}, \boldsymbol{w}) = \mathcal{L}(\boldsymbol{w}), \qquad \forall \boldsymbol{w} \in \mathcal{E} \,, \tag{2.6}$$

where the bilinear form $\mathcal{B}$ is defined as

$$\mathcal{B}(\boldsymbol{u}, \boldsymbol{w}) = \int_\Omega \boldsymbol{\epsilon}(\boldsymbol{w}) : \boldsymbol{\sigma}(\boldsymbol{u}) \, \mathrm{d}\Omega \,, \tag{2.7}$$

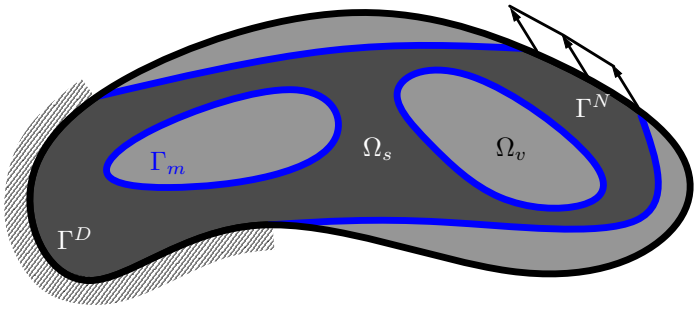

Figure 2.2: A mechanics potato to depict all relevant domains in the design domain Ω. Material domain Ω_s, void domain Ω_v, and material interface Γ_m are defined as stated in equation (2.1). Essential and natural boundary conditions, Γ^D and Γ^N respectively, are prescribed on sections of the boundary of Ω

and the linear form $\mathcal{L}$ as

$$\mathcal{L}(\boldsymbol{w}) = \int_{\Omega} \boldsymbol{w} \cdot \boldsymbol{b} \, \mathrm{d}\Omega + \int_{\Gamma_T} \boldsymbol{w} \cdot \bar{\boldsymbol{t}} \, \mathrm{d}\Gamma \ . \tag{2.8}$$

In these equations, $\boldsymbol{u}$ is the displacement and $\mathcal{E}$ is a test function space that satisfies the essential boundary condition. Furthermore, $\boldsymbol{\sigma}(\boldsymbol{u})$ follows from Hooke's law for linear elastic materials, $\boldsymbol{\sigma}(\boldsymbol{u}) = D \colon \boldsymbol{\epsilon}(\boldsymbol{u})$, where D is the constitutive tensor and $\boldsymbol{\epsilon}(\boldsymbol{w}) = (\nabla \boldsymbol{w} + \nabla \boldsymbol{u}^{\intercal})$ is the linearized strain tensor. Finally, $\boldsymbol{b}$ and $\bar{\boldsymbol{t}}$ represent body forces and boundary tractions on the domain Ω.

To solve Equation (2.6), the correct displacement field and test functions $\boldsymbol{u}$ and $\boldsymbol{w}$ need to be found. To make this more practical, the problem can be transformed into a finite-dimensional problem using a Galerkin projection. The solution to this new problem may not be exact any more. However, the domain can now be discretized and described by means of a Finite Element (FE) mesh. The resulting finite-dimensional problem is now

$$\sum_{i=m,\boldsymbol{w}} \int_{\Omega_i} \boldsymbol{\epsilon}_i(\boldsymbol{w}_i) \colon \boldsymbol{\sigma}_i(\boldsymbol{u}_i) \, \mathrm{d}\Omega = \sum_{i=m,\boldsymbol{w}} \int_{\Omega_i} \boldsymbol{w}_i \cdot \boldsymbol{b}_i \, \mathrm{d}\Omega + \int_{\Gamma} \boldsymbol{w}_i \cdot \bar{\boldsymbol{t}} \, \mathrm{d}\Gamma \ . \tag{2.9}$$

The trial solution to this problem can be written as

$$\boldsymbol{u}^h(\boldsymbol{x}) = \sum_{i \in \iota_h} N_i(\boldsymbol{x}) \mathbf{U}_i \, , \tag{2.10}$$

with shape functions N_i that interpolate the value of the solution between mesh nodes that correspond to degrees of freedom (DOFs) $\boldsymbol{U}_i$, which for an elastostatics problem represent nodal displacements. However, there is a problem with the solution given by Equation (2.10). This solution assumes the displacement field $\boldsymbol{U}$ can be accurately interpolated using shape functions N_i, which are in this case linear. But as stated in Section 2.1.1, there will be no remeshing to enable the use of a static representation of $\boldsymbol{\theta}$. This means the material interface Γ_m will cross the mesh in elements with the corresponding index set ι_c. At this crossing, there will be a discontinuity in the gradient of the displacement field, which cannot be represented by just the linear shape functions. Using this method would result in reduced accuracy of the solution to Equation (2.6).

This is where IGFEM offers an elegant solution [109]. For the elements in the index set ι_c, the location at which Γ_m crosses the element edges can be found by finding the zero of the LSF. At these locations, new nodes are placed that are part of index set ι_w, which are shown as blue circles in Figure 2.3. These nodes are associated with enriched DOFs $\boldsymbol{\alpha}_i$ and enrichment functions ψ_i. The behaviour of such a function is also illustrated in Figure 2.3. These enrichment functions are local by construction, so their contribution is only nonzero in these crossed elements. They can also describe the discontinuity in the gradient of the displacement field across Γ_m.

Every enriched node is placed along the FE mesh edges where $\phi(\boldsymbol{x}) = 0$. To ensure correct integration of the newly added enrichment functions, each crossed element in index set ι_c is subdivided into integration elements that do conform to Γ_m, while not moving the original FE mesh nodes. This means that the calculation of nodal level set values from Equation (2.5) can now be used. The enriched approximation that replaces the trial solution in Equation (2.10) is

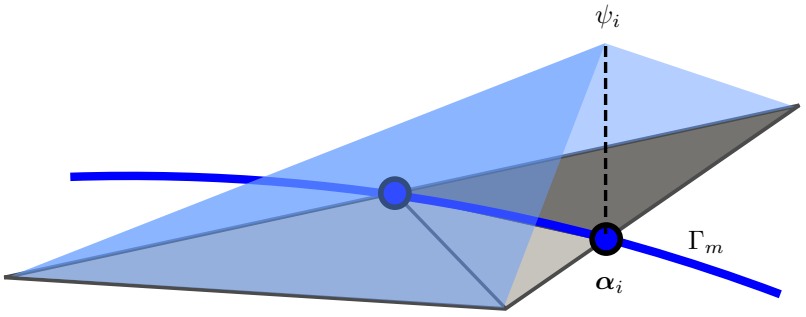

Figure 2.3: Enrichment function ψ_i in an element that is crossed by a material interface Γ_m, represented by the blue line. This function is multiplied with enriched DOF $\boldsymbol{\alpha}_i$, which corresponds to enriched node i that is represented by the blue circle. Note that the crossed element is subdivided into three integration elements that conform to Γ_m

$$\mathbf{u}^h(\boldsymbol{x}) = \sum_{i \in \iota_h} N_i(\boldsymbol{x}) \mathbf{U}_i + \sum_{i \in \iota_w} \psi_i(\boldsymbol{x}) \boldsymbol{\alpha}_i \,. \tag{2.11}$$

Now that the form of the solution is known, the elastostatic problem is transformed into a system of equations $\mathbf{KU} = \mathbf{F}$ for ease of computation. In this equation, $\mathbf{U}$ is a vector with the nodal displacements and values of the enriched DOFs. The stiffness matrix $\mathbf{K}$ and force vector $\mathbf{F}$ can be assembled using standard finite element assembly:

$$\mathbf{K} = \bigtriangleup_{i \in \iota_A} \mathbf{k}_i \,, \tag{2.12}$$

and

$$\mathbf{F} = \bigtriangleup_{i \in \iota_A} \mathbf{f}_i \,, \tag{2.13}$$

respectively. Here, $\bigtriangleup$ denotes the standard finite element assembly operator and ι_A is the index set of all integration elements and all original elements in the FE mesh that are not intersected by Γ_m. For the integration elements, assembly of $\mathbf{k}_i$ and $\mathbf{f}_i$ happens using an isoparametric procedure to map it onto its parent element that was intersected by Γ_m. In this case, the integration element's local stiffness matrix is defined as

$$\mathbf{k_e} = \int_{\triangle} j_e \mathbf{B}^\intercal \mathbf{D} \mathbf{B} \, \mathrm{d}\boldsymbol{\xi} \,. \tag{2.14}$$

In this equation, $\triangle$ is the integration element's reference triangle, j_e is the determinant of the Jacobian of the isoparametric mapping of the integration element and $\mathbf{D}$ is the material constitutive matrix. Also, $\mathbf{B}$ is the strain-displacement matrix that is defined as $\mathbf{B} = [\boldsymbol{\Delta} N_1 \; \boldsymbol{\Delta} N_2 \; \ldots \; \boldsymbol{\Delta} N_n \; \boldsymbol{\Delta} \psi_1 \; \boldsymbol{\Delta} \psi_2 \ldots \; \boldsymbol{\Delta} \psi_m]$ and $\boldsymbol{\xi}$ is the reference master coordinate of the parent element. Note that $\mathbf{B}$ is comprised two parts, one is from the n linear shape functions and the other from the m enrichment functions, the differential operator $\boldsymbol{\Delta}$ is defined as

$$\boldsymbol{\Delta}_{\boldsymbol{\xi}}^\intercal = \begin{bmatrix} \frac{\partial}{\partial x} & 0 & \frac{\partial}{\partial y} \\ 0 & \frac{\partial}{\partial y} & \frac{\partial}{\partial x} \end{bmatrix}^\intercal \,, \tag{2.15}$$

for 2D and

$$\boldsymbol{\Delta}_{\boldsymbol{\xi}}^\intercal = \begin{bmatrix} \frac{\partial}{\partial x} & 0 & 0 & 0 & \frac{\partial}{\partial z} & \frac{\partial}{\partial y} \\ 0 & \frac{\partial}{\partial y} & 0 & \frac{\partial}{\partial z} & 0 & \frac{\partial}{\partial x} \\ 0 & 0 & \frac{\partial}{\partial z} & \frac{\partial}{\partial y} & \frac{\partial}{\partial x} & 0 \end{bmatrix}^\intercal \,, \tag{2.16}$$

for 3D. The integration element's local force vector is defined as

$$\mathbf{f_e} = \int_{\triangle} j_e \begin{bmatrix} \boldsymbol{N} \\ \boldsymbol{\psi} \end{bmatrix} \boldsymbol{b} \, \mathrm{d}\boldsymbol{\xi} + \int_{\triangle \cap \Gamma^N} j_e \begin{bmatrix} \boldsymbol{N} \\ \boldsymbol{\psi} \end{bmatrix} \bar{\boldsymbol{t}} \, \mathrm{d}\boldsymbol{\xi} \,, \tag{2.17}$$

where $\boldsymbol{b}$ is the body force on the integration element and $\bar{\boldsymbol{t}}$ are the tractions working on the sides of the integration elements that intersect Γ^N. In conclusion, by using this enriched formulation, the solution of an elastostatic problem can be found with no need for remeshing of the domain to make the discretization conform to Γ_m. For more detail on the IGFEM formulation, the reader is referred to [109].

2.1.3. Topology optimization procedure with IGFEM

With a method to find the displacements, and subsequently the stresses and strains in the domain by solving $\mathbf{KU} = \mathbf{F}$, the design should be optimized using TO. In order to do this efficiently, a gradient-based optimization scheme is used [12]. In short, the following problem needs to be solved to minimize the compliance $C = \mathbf{U}^\intercal\mathbf{KU}$ of a structure:

$$\begin{aligned} \boldsymbol{s}^* = \quad & \arg\min_{\boldsymbol{s}} \mathbf{U}^\intercal\mathbf{KU}\,, \\ \text{subject to} \quad & \mathbf{KU} = \mathbf{F}\,, \\ & |\boldsymbol{s}| \leq 1\,, \\ & V_s \,/\, V_\Omega \leq V_c\,. \end{aligned} \tag{2.18}$$

For this problem, the maximum allowed magnitude of the design variables is set to 1 and a constraint is set to keep the volume fraction of the material domain in Ω, i.e. $V_s \,/\, V_\Omega$, below or equal to V_c. To find the optimal design step, the derivative of the compliance objective and volume constraint with respect to the design variables $\boldsymbol{s}$ must be found. Since the compliance objective is self-adjoint [98], the sensitivity of C with respect to design variables $\boldsymbol{s}$ can easily be found by applying the chain rule

$$\frac{\partial C}{\partial \boldsymbol{s}} = -\mathbf{U}^\intercal \frac{\partial \mathbf{K}}{\partial \boldsymbol{s}}\mathbf{U} + 2\mathbf{U}^\intercal \frac{\partial \mathbf{F}}{\partial \boldsymbol{s}}\,. \tag{2.19}$$

However, finding $\partial\mathbf{K}/\partial\boldsymbol{s}$ and $\partial\mathbf{F}/\partial\boldsymbol{s}$ is more involved. One can think of it like this: if one were to change one design variable, this would influence level set values in the vicinity of its corresponding RBF, represented by $\partial\phi_j/\partial s_i$. These changed level set values move Γ_m and thus the locations of enriched nodes that are nearby, described in the term $\partial\boldsymbol{x}_n/\partial\phi_j$. This finally changes connected integration elements' stiffness matrices and force vectors, $\partial\mathbf{k}_e/\partial\boldsymbol{x}_n$ and $\partial\mathbf{f}_e/\partial\boldsymbol{x}_n$. By applying this reasoning, the sensitivity of the compliance can be written as

$$\frac{\partial C}{\partial s_i} = \sum_{j\in\iota_i}\sum_{e\in\iota_j}\sum_{n\in\iota_n}\left(-\mathbf{u}_e^\intercal \frac{\partial \mathbf{k}_e}{\partial \boldsymbol{x}_n}\frac{\partial \boldsymbol{x}_n}{\partial \boldsymbol{\phi}_j}\mathbf{u}_e + 2\mathbf{u}_e^\intercal \frac{\partial \mathbf{f}_e}{\partial \boldsymbol{x}_n}\frac{\partial \boldsymbol{x}_n}{\partial \boldsymbol{\phi}_j}\right)\frac{\partial \boldsymbol{\phi}_j}{\partial s_i}\,. \tag{2.20}$$

In this equation, a summation is done over every conventional mesh node j where the RBF corresponding to design variable $\boldsymbol{s}_i$ is nonzero, represented by index set ι_i. For each of these nodes, a summation is done over every integration element e that is connected to node j, which corresponds to index set ι_j. Finally, for every integration element e, a summation is done over index set ι_n, which represents every enriched node in the connectivity of integration element e.

Note that the sensitivity of the objective is nonzero only in the neighbourhood of Γ_m because this is where enriched nodes are placed. A consequence of this is that all initial designs in an optimization problem must have enriched nodes, which means the void domain Ω_v may not be empty. Also, $\partial\phi_j/\partial s_i$ is the value of the RBF corresponding to design variable s_i at node j. This value can be found in matrix $\boldsymbol{\theta}$ from Equation (2.5). This value, as stated before, is calculated in advance.

From Equation (2.20), the derivative of the integration element's stiffness matrix $\mathbf{k}_e$ can be found by applying the chain rule to Equation (2.14), assuming that $\mathbf{D}$ is constant through Ω_s, resulting in

$$\frac{\partial \mathbf{k}_e}{\partial \boldsymbol{x}_n} = \int_\triangle \left(\frac{\partial j_e}{\partial \boldsymbol{x}_n}\mathbf{B}^\intercal\mathbf{D}\mathbf{B} + j_e\frac{\partial \mathbf{B}^\intercal}{\partial \boldsymbol{x}_n}\mathbf{D}\mathbf{B} + j_e\mathbf{B}^\intercal\mathbf{D}\frac{\partial \mathbf{B}}{\partial \boldsymbol{x}_n}\right)\mathrm{d}\boldsymbol{\xi}\,. \tag{2.21}$$

The derivative of the local force vector can be found similarly, which leads to

$$\frac{\partial \mathbf{f}_e}{\partial \boldsymbol{x}_n} = \int_\triangle \left(\frac{\partial j_e}{\partial \boldsymbol{x}_n}\begin{bmatrix}\boldsymbol{N}\\ \boldsymbol{\psi}\end{bmatrix}\boldsymbol{b} + j_e\begin{bmatrix}\partial\boldsymbol{N}/\partial\boldsymbol{x}_n\\ 0\end{bmatrix}\boldsymbol{b}\right)\mathrm{d}\boldsymbol{\xi} + \int_{\triangle\cap\Gamma^N}\left(\frac{\partial j_e}{\partial \boldsymbol{x}_n}\begin{bmatrix}\boldsymbol{N}\\ \boldsymbol{\psi}\end{bmatrix}\bar{\boldsymbol{t}} + j_e\begin{bmatrix}\partial\boldsymbol{N}/\partial\boldsymbol{x}_n\\ 0\end{bmatrix}\bar{\boldsymbol{t}}\right)\mathrm{d}\boldsymbol{\xi}\,. \tag{2.22}$$

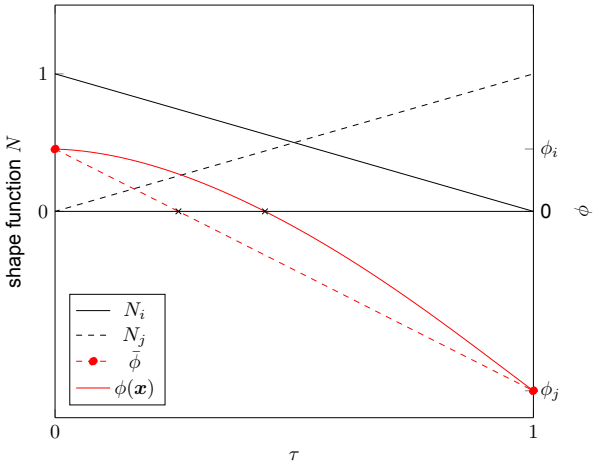

Figure 2.4: Example of the linear shape functions and the resulting linear approximation of the LSF along an element edge, compared with $\phi(\boldsymbol{x})$ itself along the same edge. The locations at which both $\bar{\phi}$ and the LSF change signs are depicted by black crosses.

Note that in the second term of each integral, the contribution of the enrichment functions is zero. This is due to the local construction of the enrichment functions, which means they are not influenced by the enriched node's location in global coordinates.

2.1.4. Linear interpolation of the LSF

The last term in Equation (2.20), is $\partial \boldsymbol{x}_n / \partial \phi_j$, which is also known as the design velocities. This term describes the movement of an enriched node on material interface Γ_m due to a change in a nodal level set value. The value of this derivative depends on the location of the enriched nodes, which are placed along every edge of elements in index set ι_c that is intersected by Γ_m. One may consider one such edge between FE mesh nodes i and j. On this edge, a normalized coordinate $\tau = \|\boldsymbol{x} - \boldsymbol{x}_i\| / \|\boldsymbol{x}_j - \boldsymbol{x}_i\|$ is defined that is zero at node i and one at node j. By using linear shape functions to interpolate between nodal level set values ϕ_i and ϕ_j, an approximation of the LSF can be made along this edge:

$$\bar{\phi}(\tau) = (1 - \tau)\, \phi_i + \tau \phi_j \,. \tag{2.23}$$

Since this element edge is intersected by Γ_m, the signs of ϕ_i and ϕ_j are opposite. At the location where the LSF is zero, an enriched node must be placed. According to the linear approximation $\bar{\phi}(\tau)$ from Equation (2.23) the normalized coordinate of the enriched node is

$$\tau_n = -\frac{\phi_i}{\phi_j - \phi_i} \,. \tag{2.24}$$

This approach is visualized in Figure 2.4. The global coordinate of this enriched node can be found with the inverse mapping between τ and $\boldsymbol{x}$, which is

$$\boldsymbol{x}_n = \boldsymbol{x}_i - \frac{\phi_i}{\phi_j - \phi_i} \left(\boldsymbol{x}_j - \boldsymbol{x}_i\right) \,. \tag{2.25}$$

Note that only after placing the enriched nodes at these locations, the discretization of the problem is complete and the representation of Γ_m can be made. This linear approximation means that differentiation of this location with respect to the nodal level set value of node i is straightforward:

$$\frac{\partial \boldsymbol{x}_n}{\partial \phi_i} = -\frac{\phi_j}{(\phi_j - \phi_i)^2} (\boldsymbol{x}_j - \boldsymbol{x}_i) \,. \tag{2.26}$$

With all terms in Equation (2.20) defined, there is gradient information for the optimizer to try and find a solution to Problem (2.18). The optimizer uses the Method of Moving Asymptotes (MMA) [115] to find the next design iteration. For this MMA, the Lagrange multiplier that is used in the subproblem to force the constraints is set to a value of 10 and a move limit is set to prevent Γ_m from moving too fast. This approach was also used by van den

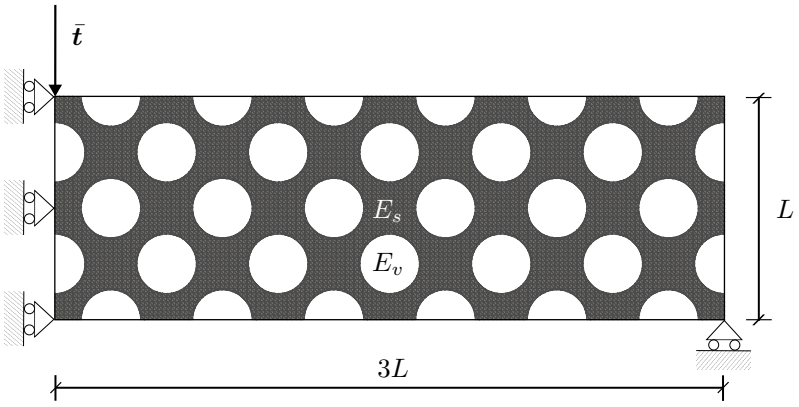

Figure 2.5: Initial design of the MBB problem. The white circular inclusions are part of Ω_v. The elements in this domain are not shown in the figure, but they are analyzed in the FEA. On the left side, a symmetry condition is applied and the same is done for a downward force $\bar{t}$ on the top-left corner. The bottom-right corner is vertically supported.

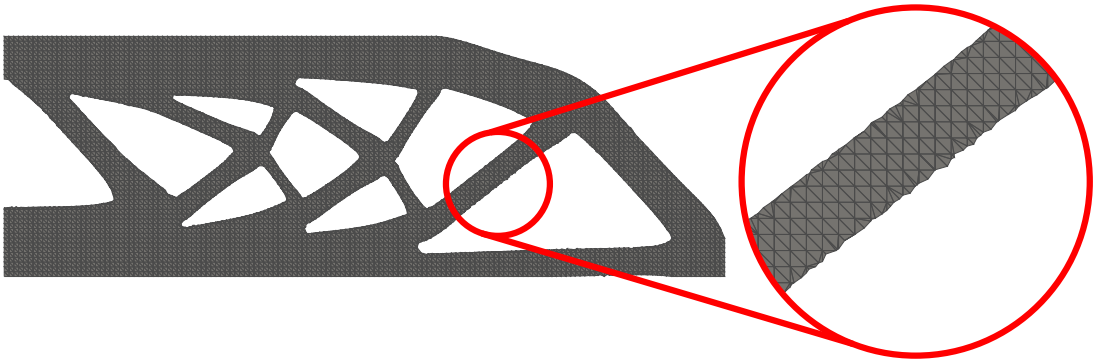

Figure 2.6: Optimized design of the MBB beam problem while using IGFEM level set-based TO, with a magnified view of the zigzagging behaviour in the representation of Γ_m. The interface should be smooth because of the use of RBFs.

Boom et al. [12] and resulted in a smoother representation of the geometry compared to density-based methods. However, their work also stated a problem regarding the surface of designs. If the number of design variables was not sufficiently reduced compared to the number FE mesh nodes, zigzagging of the material interface was visible. This zigzagging was attributed to an approximation error, with the mesh being too coarse to accurately describe the deformations and stresses in the structure. This inconsistency in the surface was, among other examples, shown for the well-known MBB beam problem.

We study this problem on a domain of size $3L \times L$. On the left side of the domain, there is a symmetry condition, while on the top-left corner a downward pointing force $\bar{t}$ is applied. The bottom-right corner of the domain is vertically supported and for the optimization problem, the maximum allowed volume $V_c = 55\%$ of the domain. The material in Ω_s has a Young's modulus $E_s = 1$ and a Poisson's ratio $\nu_s = 0.3$. The void domain Ω_v has a Young's modulus $E_v = 10^{-6}$ and the same Poisson's ratio. The mesh consists of $150 \times 50 \times 2$ triangular elements. Since the problem is most prominent when the number of design variables is not reduced, an RBF is placed at each FE mesh node. Each RBF's support radius is $r_s = \sqrt{2}a$ and the move limit set for the MMA is 0.001. The initial design is depicted in Figure 2.5. The optimized design and the reported zigzagging can be seen in Figure 2.6.

2.1.5. Improved location approximation of zeros of the LSF

By plotting the LSF along the element edges, a possible cause other than a coarse mesh can be found. As the RBFs spanning the LSF are nonlinear, the linear approximation of this function can give difficulties if the diameters of the RBFs are not sufficiently large. This can be seen by the discrepancy between the zeros of $\phi(\boldsymbol{x})$ and $\bar{\phi}$ in Figure 2.4. The use of larger RBF diameters r_s could solve this, but this approach would result in a loss of fine detail in possible designs.

A solution to this incorrect node placement could be to apply a minimization problem on $|\phi(\boldsymbol{x})|$ along the crossed element edges. Since the definition of the LSF in Equation (2.4) is smooth, this minimization problem is viable. As a proof of concept, the final design in Figure 2.6 was used to interact with the same mesh of $150 \times 50 \times 2$ triangles. However, this time the enriched nodes were not placed at the location described by Equation (2.25). Instead, the

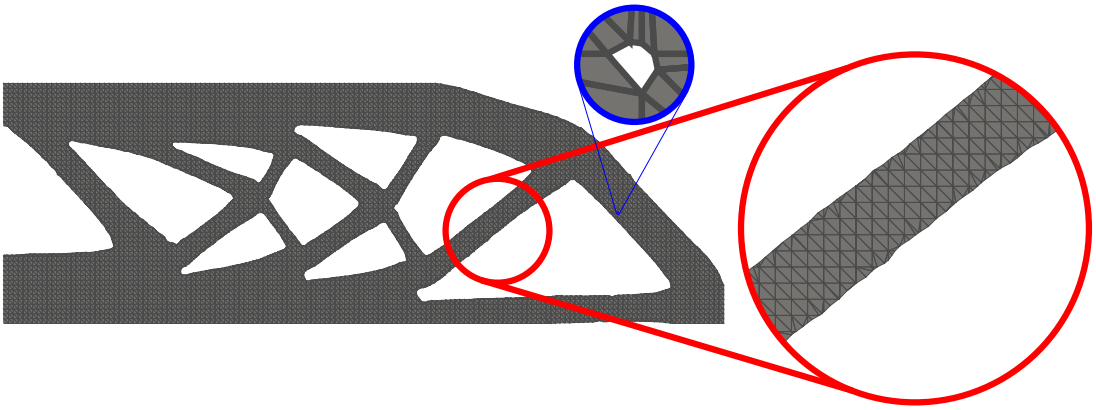

Figure 2.7: The same optimized design of the MBB problem from Figure 2.6. However, for this figure, the enriched nodes were placed at the location where $|\phi(\boldsymbol{x})|$ is minimized using the bisection method. Note the absence of the zigzagging effect. This shows that the representation of Γ_m using spanning design variables with RBFs is indeed smooth. The blue magnified view also shows a hole that has nucleated during the optimization. This hole, although smaller, is also present in Figure 2.6

bisection method was used to find the minimum of $|\phi(\boldsymbol{x})|$ along every crossed edge and an enriched node was placed at this location. The result of this approach is depicted in Figure 2.7 and it shows that indeed the new representation of the material interface Γ_m is smoother than before.

However, an approach based on minimization methods is not differentiable with respect to a nodal level set value and thus design velocities cannot be calculated this way. An alternative is to add an extra control point k at the midpoint of each element edge to set up a quadratic approximation of the LSF instead of the linear one in Equation (2.23). The value of the LSF at these locations follows from Equation (2.4). Moreover, because the locations of these midpoints are fixed, the relation between their level set value and the design variables can be stored in a matrix in the same manner as in Equation (2.5). With this extra control point and corresponding ϕ_k, a new normalized coordinate ζ is introduced that now is -1 at node i while it still is 1 at node j. This new mapping is defined as

$$\zeta(\boldsymbol{x}) = 2\frac{|\boldsymbol{x} - \boldsymbol{x}_i|}{|\boldsymbol{x}_j - \boldsymbol{x}_i|} - 1\,. \tag{2.27}$$

With the new mapping, quadratic shape functions can be used to interpolate the nodal level set values, so that the quadratic approximation of the LSF along the element edge is

$$\hat{\phi}(\zeta) = \frac{\zeta(\zeta-1)}{2}\phi_i - (\zeta+1)(\zeta-1)\phi_k + \frac{\zeta(\zeta+1)}{2}\phi_j\,. \tag{2.28}$$

Note that this can be expressed in the form $a\zeta^2 + b\zeta + c$, the zeros of which are $\zeta_n = \left(-b \pm \sqrt{b^2 - 4ac}\right)/(2a)$. Moreover, this quadratic approximation can have at most two of these zeros. If ϕ_i and ϕ_j have opposite signs, there can only be one zero along the element edge. As before, if there is a sign change detected along an element edge, an enriched node must be placed. This time the enriched node is placed at the location where $\hat{\phi}(\zeta) = 0$, which is at the locations

$$\zeta_n = \frac{-\phi_i + \phi_j \pm \sqrt{8\phi_k\left(-\phi_i - \phi_j + 2\phi_k\right) + \left(\phi_i - \phi_j\right)^2}}{2\left(-\phi_i - \phi_j + 2\phi_k\right)}\,. \tag{2.29}$$

Since only one of these zeros is on the element edge, i.e. $-1 \leq \zeta_n \leq 1$, the enriched node is placed at the location that satisfies this condition. The global location of this enriched node $\boldsymbol{x}_n$ and its partial derivatives with respect to the nodal level set values ϕ_i, ϕ_j and ϕ_k are trivial to find, and are stated in Appendix A. A problem that arises is that the extra derivative $\partial\boldsymbol{x}_n/\partial\phi_k$ cannot be added directly to the sensitivity of the objective. The midpoints do not correspond to shape functions in the mesh, which means ι_j in Equation (2.20) is empty and there are no integration elements in the support of these nodes. However, every midpoint k is by definition on the edge between nodes i and j. Thus the integration elements in the support of point k, represented by index set ι_m, can be considered to be the intersection of the supports of nodes i and j (i.e., $\iota_m = \mathrm{supp}(N_i) \cap \mathrm{supp}(N_j)$). To add the contribution of the new control point to the sensitivities, a summation must be done over every midpoint in index set ι_k at which the RBF corresponding to design variable s_i is nonzero. For every midpoint m in this set, a summation is done

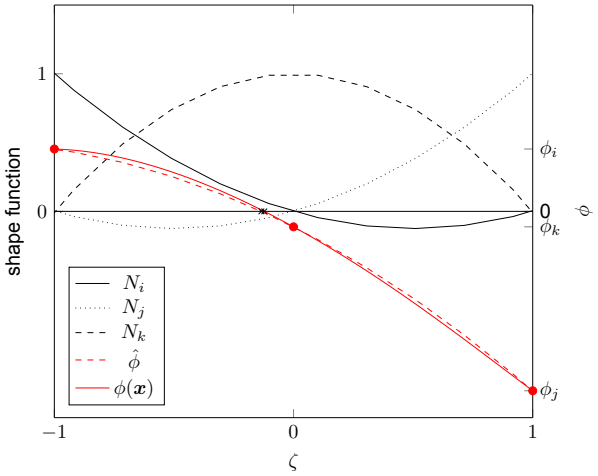

Figure 2.8: The quadratic shape functions and the resulting quadratic approximation $\hat{\phi}$ of the LSF along an element edge, compared with $\phi(\boldsymbol{x})$ along the same edge. The zeros of both the LSF and $\hat{\phi}$ are again depicted by black crosses. However, the new location of the enriched node is closer to the exact zero compared to the linear approximation of the same element edge in Figure 2.4.

over all integration elements e in index set ι_m. With this reasoning, the compliance objective's sensitivity when using a more quadratic approximation of the LSF to place enriched nodes is

$$\begin{aligned}\frac{\partial C}{\partial s_i} = &\sum_{j\in\iota_i}\sum_{e\in\iota_j}\sum_{n\in\iota_n}\left(-\mathbf{u}_e^\intercal\frac{\partial \mathbf{k}_e}{\partial \boldsymbol{x}_n}\frac{\partial \boldsymbol{x}_n}{\partial \boldsymbol{\phi}_j}\mathbf{u}_e + 2\mathbf{u}_e^\intercal\frac{\partial \mathbf{f}_e}{\partial \boldsymbol{x}_n}\frac{\partial \boldsymbol{x}_n}{\partial \boldsymbol{\phi}_j}\right)\frac{\partial \boldsymbol{\phi}_j}{\partial s_i} + \\ &\sum_{m\in\iota_k}\sum_{e\in\iota_m}\sum_{n\in\iota_n}\left(-\mathbf{u}_e^\intercal\frac{\partial \mathbf{k}_e}{\partial \boldsymbol{x}_n}\frac{\partial \boldsymbol{x}_n}{\partial \phi_m}\mathbf{u}_e + 2\mathbf{u}_e^\intercal\frac{\partial \mathbf{f}_e}{\partial \boldsymbol{x}_n}\frac{\partial \boldsymbol{x}_n}{\partial \phi_m}\right)\frac{\partial \phi_m}{\partial s_i}\,.\end{aligned} \tag{2.30}$$

2.1.6. Verification of the analytical sensitivities

To verify the implementation of this new enriched node placement and the subsequent addition to the objective sensitivities, the analytically computed sensitivities $\partial C/\partial s_i$ are compared to numerically computed central finite differences C_i'. This comparison is done by finding the relative differences δ_i between the two. This is done for multiple design variables with nonzero sensitivities and a range of step sizes. The relative differences are defined as

$$\delta_i = \frac{C_i' - \partial C/\partial s_i}{\partial C/\partial s_i}\,. \tag{2.31}$$

This comparison is conducted on a simple problem that was also used by van den Boom et al. [12]. In this problem, a $2L \times L$ domain is optimized, the domain is visualized in Figure 2.9. This domain is fixed on the left side and a downward pointing force $\bar{\boldsymbol{t}}$ is applied to the bottom right corner. The FE mesh consists of $12 \times 6 \times 2$ triangular elements that are placed in a point-symmetric manner around the middle of the domain. The initial design's void domain consists of 3 circular holes. The RBF's support radius is $r_s = \sqrt{2}a$, where a is the diameter of the largest circle that can fit inside any of the triangular elements. The material in Ω_s has a Young's modulus $E_s = 1$ and a Poisson's ratio $\nu_s = 0.3$. The void domain Ω_v has a Young's modulus $E_v = 10^{-6}$ and the same Poisson's ratio.

The result of this finite difference analysis with the new enriched node placement can be seen in Figure 2.10. It is visible that this new method of enriched node placement yields sensitivities that have a region of step sizes where these sensitivities converge to their counterpart that are found by means of central finite differences. This means that the sensitivities introduced in Equation (2.30) to the objective sensitivities yield correct results and this improved method of enriched node placement can be used for TO in combination with level set-based IGFEM.

2.1.7. Application to the MBB beam problem

Following this result, the new approach is applied to the same MBB beam problem, so that the final design can be compared to the one shown in Figure 2.6. The final design of this optimization problem with the new enriched node placement can be seen in Figure 2.11. It shows that the representation of Γ_m is indeed smoother than before.

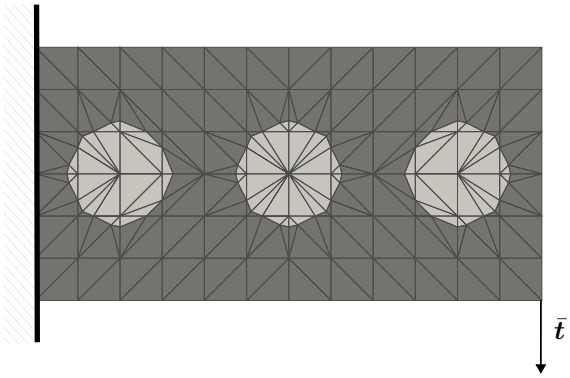

Figure 2.9: Simple problem for comparing the analytically computed sensitivities $\partial C/\partial s_i$ with the central finite differences $C_i^{'}$. Nodes on the left edge of Ω are fixed, while a downward pointing force is applied on the bottom-right corner of the domain. The elements that are light grey are part of the void domain Ω_v.

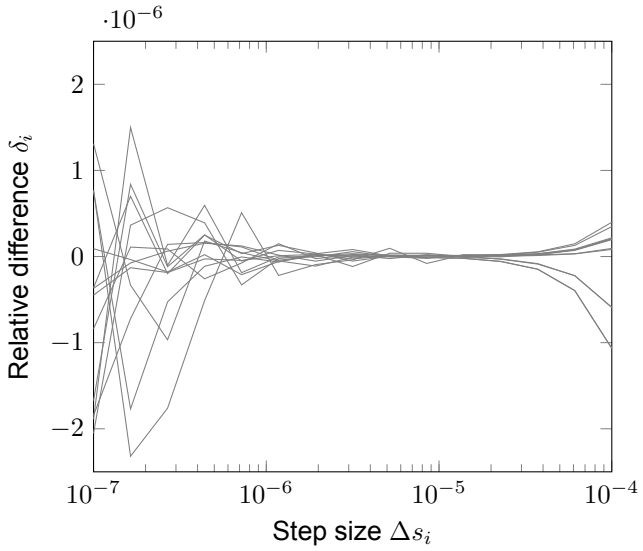

Figure 2.10: Relative differences δ_i as a function of the step size Δs_i for the numerically computed central finite differences $C_i^{'}$. The definition of δ_i can be found in Equation (2.31).

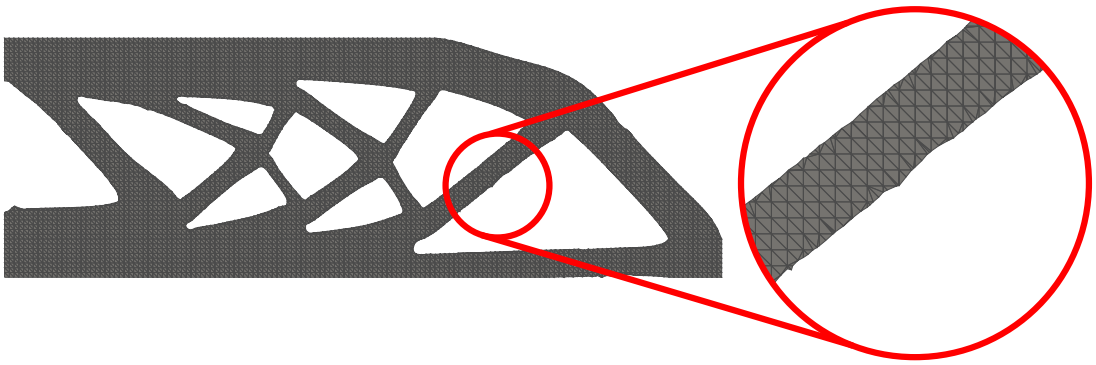

Figure 2.11: Final design of the MBB beam problem with the improved method of enriched node placement using a quadratic approximation of the LSF. Included is a magnified view of the reduction of the zigzagging behaviour in the representation of Γ_m.

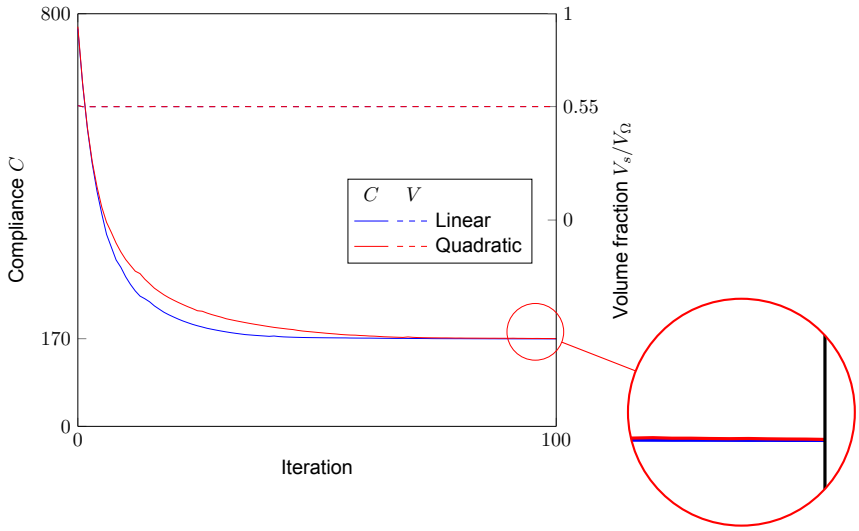

Figure 2.12: The convergence behaviour of optimizations with the linear and quadratic methods of enriched node placement applied to the MBB beam problem. Note that the optimization that uses a linear approximation of the LSF converges slightly quicker and has a slightly lower compliance C.

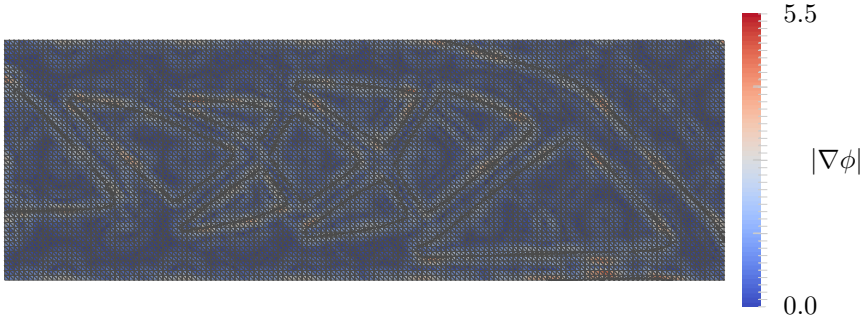

Figure 2.13: Magnitude of the gradient of the LSF for the design in Figure 2.11. The uneven colouring indicates the existence of peaks and valleys in the LSF.

However, there is still some zigzagging visible in the optimized design. Even the proposed, more advanced approximation of the location at which enriched nodes need to be placed, can be insufficient on some FE mesh edges in Ω. This suggests that in some regions the LSF still behaves too erratic. The convergence behaviour for this optimization problem with both linear and quadratic enriched node placement can be seen in Figure 2.12. It is worth mentioning that the initial design in Figure 2.5 occupies almost exactly $55\,\%$ of the design. This means that for both optimizations, the volume fraction is almost constant. One can also see that the newly proposed method is converging slightly slower towards the minimized compliance. Moreover, the final compliance with this quadratic enriched node placement is slightly higher than its linear counterpart. This can be seen in the magnified view in the bottom-right corner of the figure.

2.1.8. Regularization of the LSF

Apart from the remaining, although reduced, zigzagging, there is another problem that remains. During the optimization process, sometimes new holes are nucleated, which can be seen in Figure 2.7 and has been reported in literature as a feature in some level set methods [76]. However, in the method used in this work should not be able to create these new holes [12]. This is supported by Equation (2.20), where the sensitivity is dependent on the derivative of the location of enriched nodes with respect to nodal level set values. This implies that sensitivities are only nonzero in the vicinity of Γ_m. Thus the interface can only be moved and not created in the domain without the use of for example topological derivatives [2]. This means that the nucleation of these holes is a numerical artefact. A cause of this behaviour can be found when analyzing the magnitude of the gradient of the nodal level set values $\nabla\phi = [\partial\phi/\partial x,\ \partial\phi/\partial y]$ in the final design from Figure 2.11. This plot of $|\nabla\phi|$ which can be seen in Figure 2.13.

The patches in $|\nabla\phi|$ indicate variations in the field, which correspond to peaks and valleys in the LSF itself. These local extrema push or pull the material interface, which is undesired. When comparing this figure to Figure 2.14,

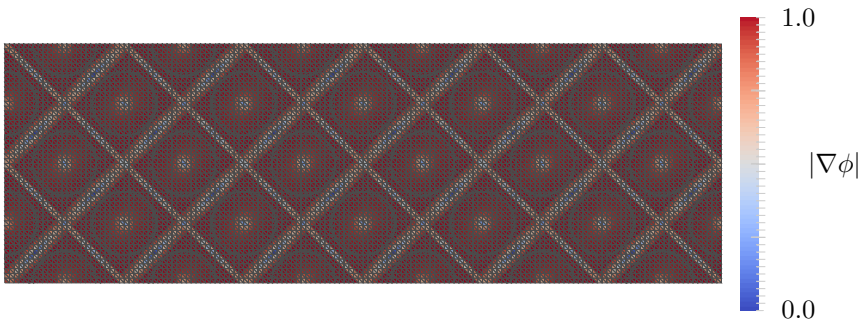

Figure 2.14: Magnitude of the gradient of the LSF for the initial design of the MBB beam problem in Figure 2.5. Note that all values of $|\nabla\phi|$ in the neighbourhood of Γ_m are equal to 1, indicating a more well-posed problem.

where the same field has been plotted for the initial design of the MBB beam, one can see that this is not initially the case. Here, one can see the LSF in another light. $|\nabla\phi| = 1$ through the whole domain, except in the middle of the initial voids and in locations that are equidistant to multiple void centres. This constant gradient indicates that the magnitude of the LSF keeps increasing when moving away from the material interface Γ_m. Because of this property, $\phi(\boldsymbol{x})$ can also be seen as the signed distance from any location $\boldsymbol{x}$ to Γ_m. However, as the MMA starts changing the design variables to minimize the objective function, the LSF appears to lose this property. This irregular gradient has been reported to cause problems during the optimization, like convergence to suboptimal local minima [24] and numerical artifacts [121]. Furthermore, the gradient of the LSF along the zero-level contour can heavily influence the convergence rate of the optimization process [1, 23].

One solution that has been suggested is the application of a regularization scheme on the LSF or its sensitivities. A range of these methods have been reported in literature [40, 24, 74]. In this work, regularization by means of reinitialization of the LSF is used to maintain the physical meaning of nodal level set values and make it a signed distance function with $|\nabla\phi| = 1$ again [125]. One exception to this is further away from the material interface. The signed distance function is clipped above and below the threshold of $\pm 4a$, where a is again the diameter of the largest circle that can fit inside any of the triangular elements. This clipping prevents excessively large nodal level set values, thus avoiding design variables outside the bounds set in Problem (2.18) and keeping the MMA from having to enforce this constraint.

Because of the IGFEM formulation, this method is fairly straightforward to implement. During the subdivision of elements that are crossed by Γ_m into integration elements, lower dimensional elements are created that conform to the material interface. These elements can be used to apply immersed boundary conditions [11]. Because of these elements, the updated nodal level set value at every FE mesh node can be defined as the smallest distance from this node to its projection on any lower-dimensional element along Γ_m. This updated set of level set values can then be updated into design variables by solving Equation (2.5) while using the newly updated vector $\boldsymbol{\phi}$. Although this method of regularization is relatively straightforward, it is computationally expensive. Because of this reason, the decision was taken to reinitialize the LSF only periodically. Another reason to take this approach is to change the interface as little as possible. If the number of design variables is less than the number of FE mesh nodes, not every combination of level set values can be represented by the design variables. This means there is a risk of not preserving the zero-level set contour. Reducing the frequency of reinitialization steps minimizes the risk of negative effects that it could cause.

To test this method of regularization of the LSF, the same MBB beam problem from Figure 2.5 was solved while applying different reinitialization frequencies. Reinitialization happened every 5, 10, 15 and 20 iterations and, as before, the optimization was terminated after 100 iterations. For these final designs in Figure 2.15, another advantage can be seen: the material interface is even smoother than that seen in Figure 2.11. This indicates that the regularization results in a smoother LSF, which means that enriched nodes can be placed more accurately along element edges that are intersected by the zero contour of the LSF. However, Figure 2.15a also shows that reinitializing the LSF too frequently can have a detrimental effect as well. During this optimization, an extra strut is added to the structure on the left side of the domain. On the other hand, Figure 2.15d shows the uncontrolled nucleation of a new hole again, which is also visible in Figure 2.7. This indicates that a reinitialization interval of 20 iterations is too large to prevent the nucleation of new holes.

From the convergence behaviour of these optimizations, as seen in Figure 2.16, it can be concluded that reinitialization of the LSF does indeed result in quicker convergence. Moreover, when this regularization method is combined with the enriched node placement that was introduced in Section 2.1.5, the result is a very smooth representation of Γ_m. This is the case even for problems for which an RBF is placed at every FE mesh node, although this could help in smoothing out the material interface even further. Although the designs in Figure 2.15b and Figure 2.15c

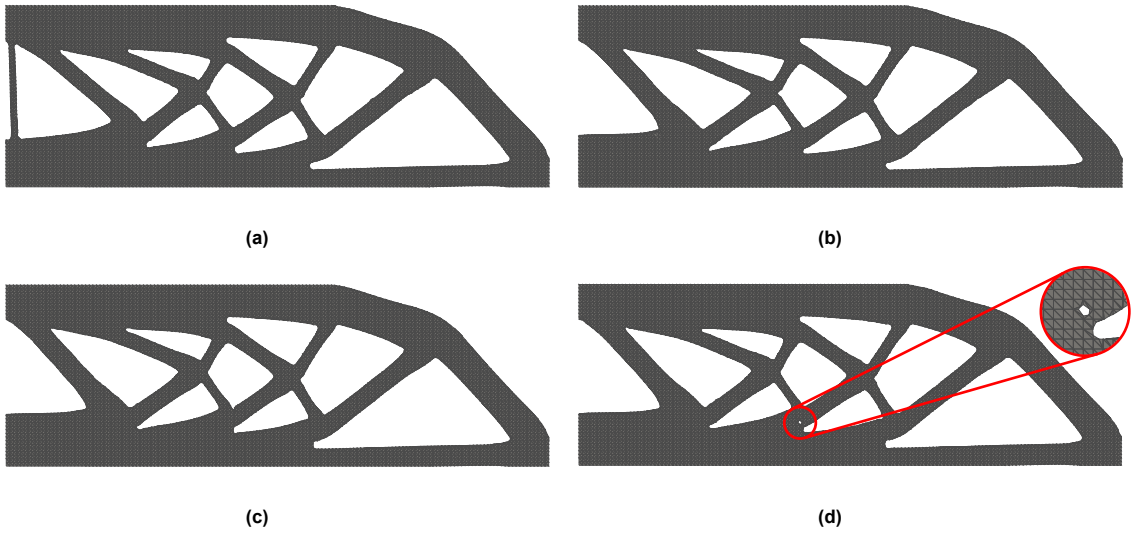

Figure 2.15: Final results of the MBB beam problem from Figure 2.5 while using regularization by means of periodic reinitialization of the LSF. All optimizations used the improved method of enriched node placement. **(a)** shows that an interval of 5 iterations results in an additional strut in the design. **(b)** and **(c)** depict the optimized design with an interval of 5 and 10 iterations, respectively. Both of these designs look similar with a smooth material interface and no traces of newly nucleated holes. **(d)** shows that a reinitialization interval of 20 iteration is not enough to prevent the nucleation of new holes. This new hole is highlighted in the magnified view in red.

are very similar, because of computational cost, a reinitialization interval of 15 iterations is used as a valid choice for this problem. Although it is problem-dependent, this interval is also used for other other optimization problems that are solved in this work.

To prove that the LSF of the optimized design is indeed more smooth with the proposed regularization, $|\nabla\phi|$ of the design in Figure 2.15c is visualized in Figure 2.17. This figure shows the impact of the reinitialization scheme on the LSF. As before in Figure 2.14, $|\nabla\phi| = 1$ everywhere in the neighbourhood of the discontinuity, except at points that are equidistant to multiple material interfaces. Also, $\nabla\phi = 0$ at points where ϕ has been clipped, which is at locations that are further away from Γ_m. Because this happens at locations far from the material interface, it will not influence the sensitivities in any way.

2.1.9. Application to a 3D cantilever beam

Now that the correct implementation of this improved representation of the material interface in two-dimensional problems has been proven, this same approach is applied to a three-dimensional problem. The compliance minimization problem given by Equation (2.18) is solved on a $2L \times L \times 0.5L$ cantilever beam. This domain is discretized using a mesh consisting of $40 \times 20 \times 10 \times 6$ tetrahedral elements, which are placed so that the mesh is symmetric across its yz plane. Also, the influence of 1848 design variables is spanned by $22 \times 12 \times 7$ RBFs with a radius $r_s = \sqrt{2}a$. Here, a is the diameter of the largest sphere that can be placed in any of the tetrahedral elements. The displacements of all nodes at $x = 0$ are set to zero and a distributed line load with $|\bar{\boldsymbol{t}}| = 0.2$ per unit length is applied to the nodes at $x = 2 \times L \cap y = 0$. All elements in Ω_s were given a Young's modulus $E_s = 1$ and a Poisson's ratio $\nu_s = 0.3$. Similar to the two-dimensional problems before, the material properties in the void domain are $E_v = 10^{-6}$ and $\nu_v = 0.3$. The maximum allowed volume in the material domain Ω_s is $V_c = 40\%$ of the design domain Ω. The voids in the initial design of this problem are shown in Figure 2.18. The move limit of the MMA is set to 0.001 and the optimization was terminated after 100 iterations.

This optimization problem was solved twice. As a reference, it was first solved while placing enriched nodes using a linear approximation of the LSF. The resulting optimized design can be seen in Figure 2.19. In the magnified view of this figure, one can see a large number of small indentations in this section of the material interface. Contrary to the zigzagging in Figure 2.6, these dimples appear periodically. Also, note the presence of a spike at the top of the magnified view. This is caused by the error in the enriched node placement, which results in erroneous sensitivities in the second to last design iteration. Because of this, the nodal level set value at the tip of the spike is negative in the final design. Because of errors in the enriched node placement, this negative level set value is interpreted as a spike. These errors in the approximation of the material interface in Figure 2.19 are similar to those in the 2D designs. An important difference, however, is that this occurs while the number of design variables is already smaller than the number of FE mesh nodes.

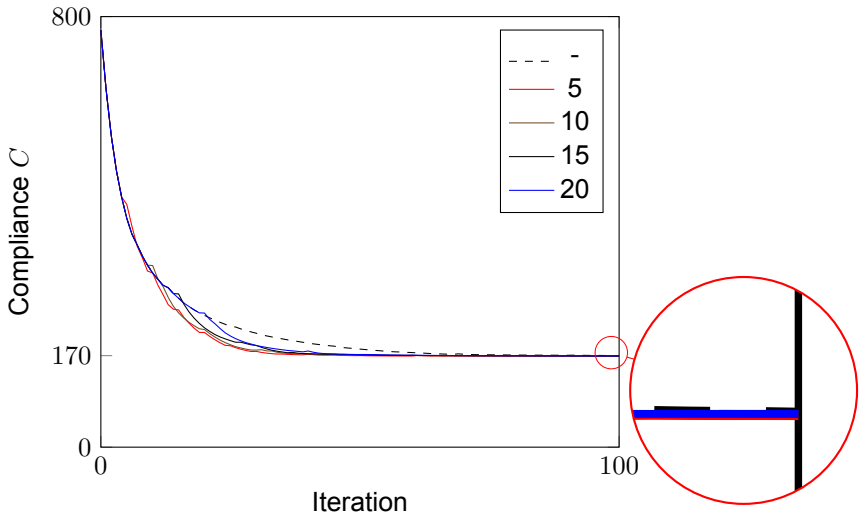

Figure 2.16: The convergence behaviour of the MBB beam problem that is described in Figure 2.5, optimized with different intervals between reinitialization. All optimizations in this plot used the placement of enriched nodes according to the improved quadratic approximation of the LSF. Note that the reinitialization scheme has a positive effect on the convergence of the objective C. The convergence behaviour of the volume constraint is not shown, since it behaves the same as in Figure 2.12.

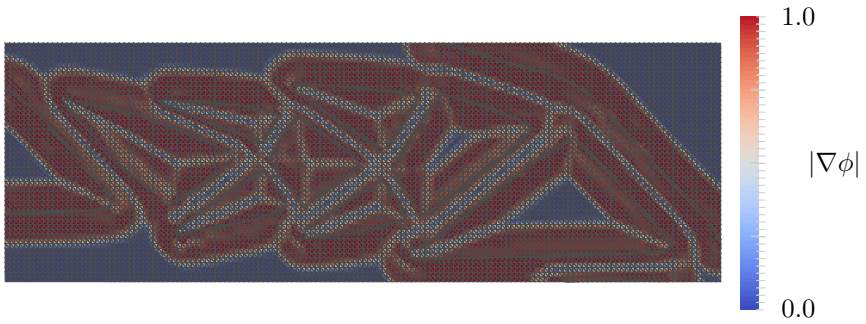

Figure 2.17: Magnitude of the gradient of the LSF for the final design of the MBB beam problem in Figure 2.5. Note that all values of $|\nabla\phi|$ in the neighbourhood of Γ_m are equal to 1. This not only makes the optimization more well-posed, it also makes reliable enriched node placement easier.

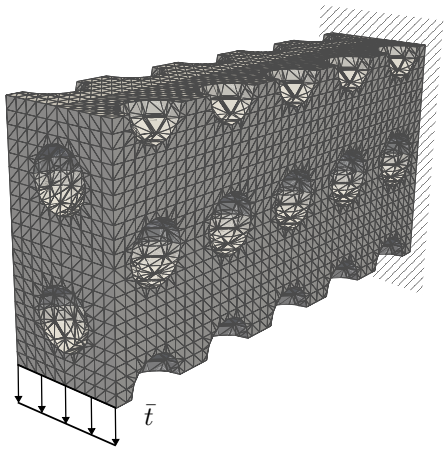

Figure 2.18: Initial design of the three-dimensional cantilever beam design problem. On the right side, at $x = 0$, the beam is fixed. On the bottom-left edge, where $x = 2 \times L \cap y = 0$, a downward load is applied.

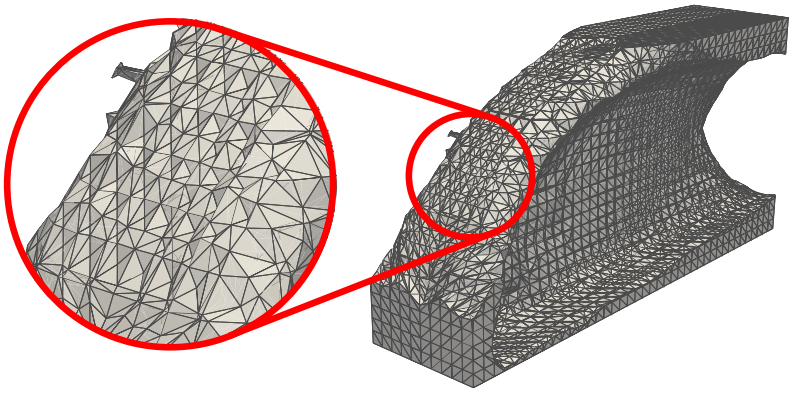

Figure 2.19: Optimized design for the three-dimensional cantilever beam problem, while using a linear approximation of the LSF to place the enriched nodes. The magnified view shows small indentations on the slanted section of the design. Also visible at the top of the magnified view is a spike that is a result of the error in the placement of enriched nodes, which in turn results in erroneous sensitivities.

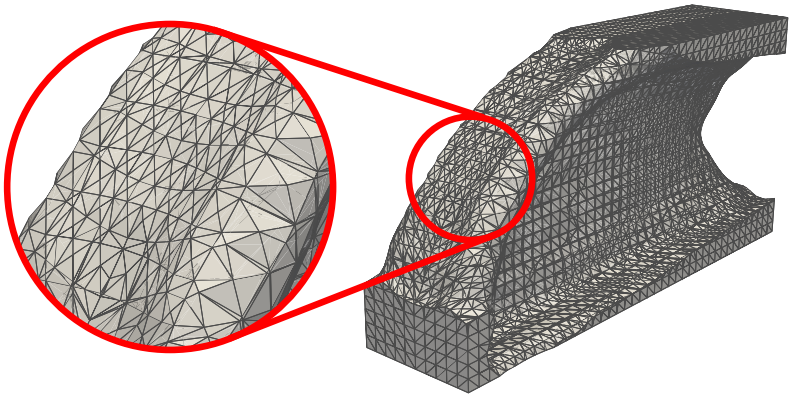

Figure 2.20: Optimized design for the problem that was shown in Figure 2.18. This geometry is the result of a quadratic approximation of the LSF along crossed element edges, while the LSF was reinitialized every 15^{th} iteration. The magnified view shows that the slanted section that had indentations in Figure 2.19 is completely smooth with this improved approach.

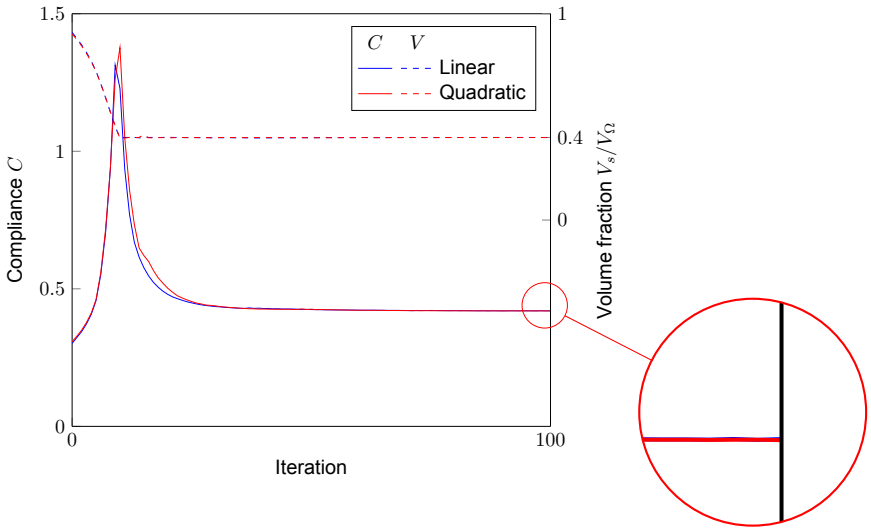

Figure 2.21: Convergence behaviour of the compliance C and volume ratio V_s/V_Ω of the optimizations with final designs shown in Figures 2.19 and 2.20. These use linear enriched node placement and quadratic enriched nodes placement in combination with a reinitialization that was executed every 15$^{\text{th}}$ iteration, respectively.

The second time the problem was solved, the improved quadratic method to approximate Γ_m was used in combination with reinitialization of the LSF that occurred every 15$^{\text{th}}$ iteration. The optimized design with this approach is shown in Figure 2.20. Contrary to the geometry in Figure 2.19, this design is very smooth in all regions of the design. This indicates that the indentations and spikes in Figure 2.19 were indeed caused by an error in the approximation of the zero of the LSF along element edges. The convergence behaviour of both optimization problems can be seen in Figure 2.16 and shows that the progression of both the objective and the volume is very similar for both approaches. In conclusion, the improvements by using a quadratic approximation of the LSF to place enriched nodes in combination with a periodic reinitialization of the same function result in significant improvements. Not only is the material interface approximated more accurately and thus becomes smoother. Also, the optimization scheme is also more reliable since the LSF now has a constant gradient in the neighbourhood of Γ_m, making the optimization problem more well-posed.

2.2. Applying IGFEM level set-based TO on the mandible

2.2.1. Voxelization of irregularly-shaped domains

All design domains Ω up to this point have been rectangular. This means that the meshes that discretized these domains could be composed of rectangles or cuboids, which can be divided into triangles or tetrahedra, respectively. Because the corners of these geometries are spaced very regularly, this type of mesh is very suitable as a basis from which to span RBFs. These types of meshes are suitable for this purpose since the centre of each RBF must be placed relatively regularly. This is needed to ensure an accurate approximation of the field that is spanned [34], which for this work, is the LSF. However, for many practical problems, Ω cannot be represented using a cuboid or rectangle. To form a mesh that does conform to Ω in such a shape, the elements in this mesh will be of different shapes and sizes. The resulting set of irregularly spaced nodes in such a mesh is thus less suitable as a basis for the RBFs.

In the definition of the sensitivities of IGFEM-based level set topology optimization in this work, there lies another problem in the use of irregularly spaced RBFs. In Equations (2.20) and (2.30), the derivative of the objective with respect to a nodal level set value is found. This value $\partial C/\partial \phi_j$ is then multiplied with $\partial \phi_j/\partial s_i$, which corresponds to the relevant value in matrix $\boldsymbol{\theta}^{\mathsf{T}}$ from Equation (2.5). This results in the sensitivity of the compliance with respect to design variable s_i. Note that in Equations (2.20) and (2.30), a summation is done over index set ι_i, which represents every mesh node j where the RBF corresponding to design variable s_i is nonzero. In a region where the mesh that discretizes Ω is finer, this index set will be larger than in other locations, thus increasing the sensitivity in such an area. The full extent of this problem can be visualized by applying such a situation to a simple problem. In Figure 2.22, the MBB beam problem is shown again. The exception is, this time the top-right corner of the domain is rounded. Moreover, the mesh is refined in the proximity of the bottom-right corner, this could be required to more accurately describe stresses and strains near the support in this corner. The resulting mesh consists of 8403 triangular elements and 4350 nodes. As before, the radius of each RBF is $\sqrt{2}a$ where a is the diameter of the largest circle that can be fitted in the largest element of the mesh

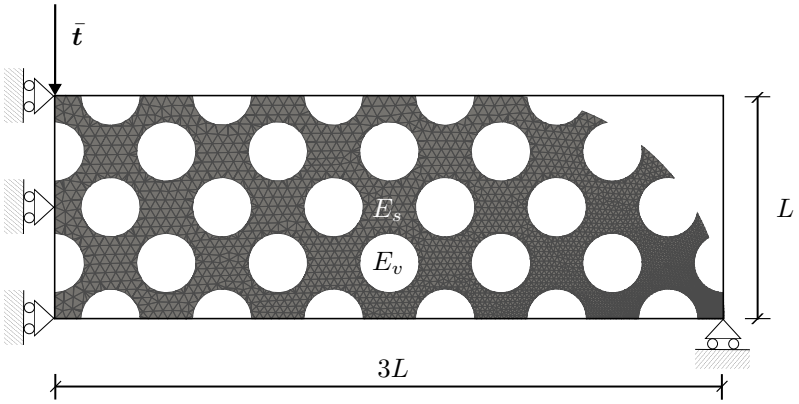

Figure 2.22: Initial design of the MBB problem, now with the top-right corner of the domain being rounded. The same boundary conditions as in Figure 2.5 are applied. Also, the domain is discretized with a variable mesh size, with the elements becoming smaller near the bottom-right corner.

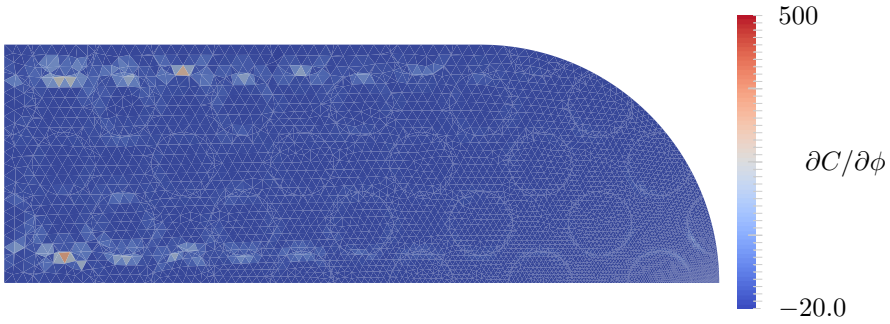

Figure 2.23: The derivative of the compliance objective C with respect to the nodal level set values.

In Figure 2.23, the derivative of the compliance with respect to the nodal level set values is shown, which appears to be independent of the element size in the region. However, the multiplication with $\partial \phi_j / \partial s_i$ from Equation (2.30) transforms this to $\partial C / \partial s_i$, which can be seen in Figure 2.24.

In Figure 2.24, it can be seen that the concentration of RBFs in the refined region of the mesh has a significant influence on the sensitivity of the compliance objective. If this gradient information were to be used by the MMA it would change the design variables according to these sensitivities. However, since each design variable in the bottom right corner influences more FE mesh nodes than elsewhere in the mesh, the LSF is changed even more in this region. This will result in the material interface being moved more rapidly in regions where the mesh is finer. However, this does not result in an optimal update strategy of the design variables for this problem.

To correct this exaggerated movement of the material interface, Ω is turned into a discrete grid of rectangles, which are called pixels and voxels in 2D and 3D, respectively. However, for the purposes of this work, the term voxels will be used in 2D as well. As discussed before, the corners of rectangles and cuboids form a very suitable basis for the RBFs. To voxelize the mesh efficiently, all nodes of the FE mesh are used as a point cloud. Around this cloud, a bounding box is created which in turn is subdivided into voxels of a specified size. However, if there are no FE mesh nodes in the vicinity of a voxel, it can be eliminated because the RBFs corresponding to its corners are zero at these nodes. To reduce the computational cost of this disposal of empty voxels, a k-dimensional tree is used to partition the design domain [31]. The resulting voxelized mesh that represents Ω with a voxel size of $0.1L$ and subsequently 328 design variables can be seen in Figure 2.25. Although the concentration of FE mesh nodes results in a local maximum in the compliance sensitivity in the bottom-right corner of the domain, there is no concentration of RBFs in this region. This means that, contrary to before, the subsequent change in the design variables will not result in an even larger change in the LSF.

The final design of the problem described in Figure 2.22 can be seen in Figure 2.26. To obtain this result, the nodes from the voxelized mesh in Figure 2.25 were used as a basis for the RBFs. The diameter was again $\sqrt{2}a$, where a is the largest circle that can be fitted in this voxelized mesh. Regularization of the LSF occurred every 15^{th} iteration and the optimization was terminated after 100 iterations. The final design in Figure 2.26 is different from other results in this work, since for this example only 328 design variables were used. This is a lot less than

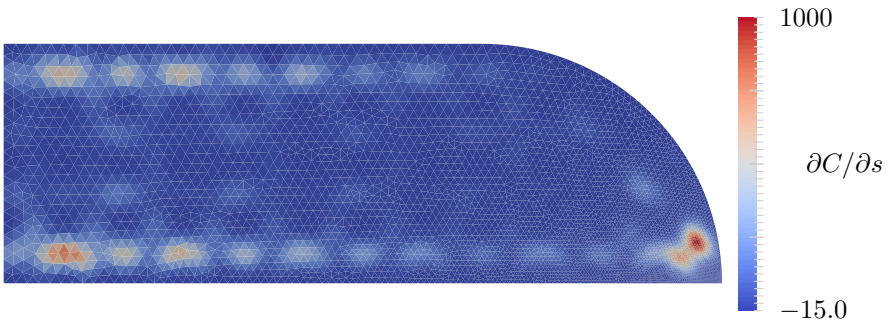

Figure 2.24: Sensitivity of the compliance objective C when RBFs are placed at every FE mesh node in a mesh with varying element sizes. Note the sudden peak in sensitivity that was not present in Figure 2.23

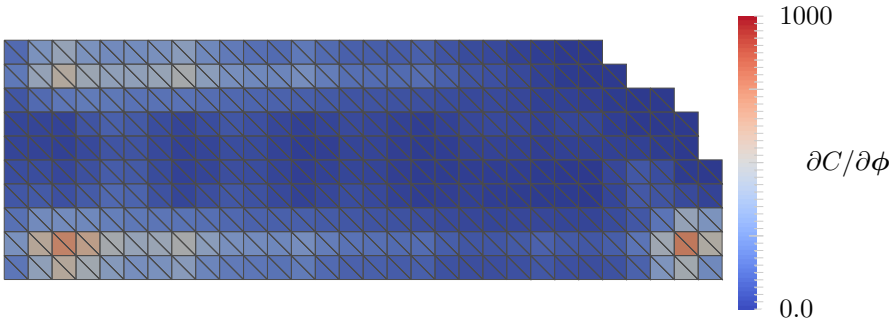

Figure 2.25: Sensitivity of the compliance objective C for a voxelized RBF mesh. Note that the field looks similar to that in Figure 2.24. However, there will be no concentration of RBFs to exaggerate the movement of the material interface in the bottom-right corner.

the 7701 design variables that were used for the final designs of Figure 2.15, resulting in a design with fewer fine details. However, the design does look similar and it also corresponds to results that were found with a similar number of design variables [12]. This means the approach of voxelizing Ω can be used as a basis for RBFs to optimize any domain in either two or three-dimensional problems.

2.2.2. Meshing of the mandible

With the optimization scheme having been validated, improved upon, and made suitable for design domains of any shape, it can be applied to the elastostatic problem of the mandible during typical clenching tasks. The starting point of this problem is a 3D scan of a damaged mandible, as depicted in Figure 2.27a. As highlighted, this mandible has a defect on the right side that compromises its structural integrity. The damaged section has to be removed with extra margins by means of resection, the cutting planes of which will connect the bone to the design domain. The resulting defect is shown in Figure 2.27b, which has a width of at least $71.33\,\mathrm{mm}$.

Since Ω describes boundaries for possible designs of the reconstruction plate, this volume should be designed with care. For this work, the focus was put on the possibility of maintaining symmetry of the facial contour. Thus the

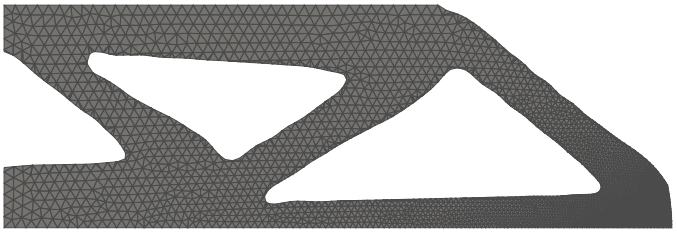

Figure 2.26: Optimized design of the problem in Figure 2.22, while using the nodes from the voxelized mesh in Figure 2.25 as a basis from which to span the RBFs.

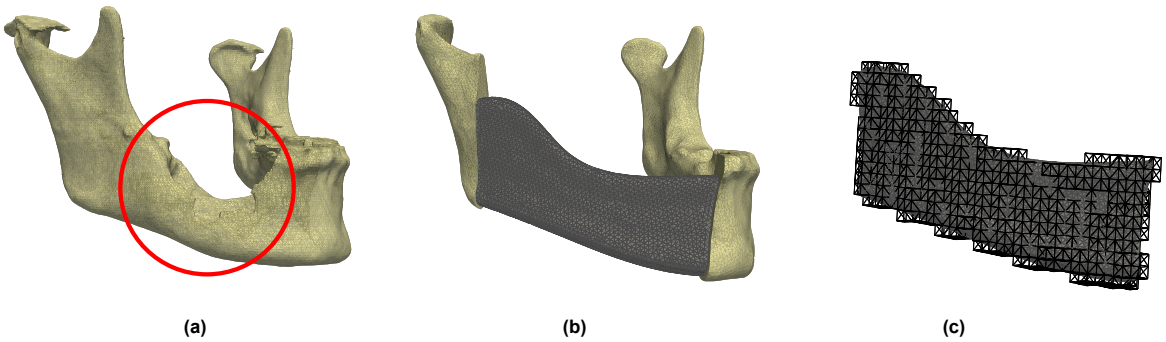

(a) (b) (c)

Figure 2.27: The approach that is taken to yield the design domain, shown in multiple steps. **(a)** shows a scan that represents the damaged mandible with the defect due to pressure-induced bone necrosis highlighted in red. **(b)** depicts the cleaned up scan and the osteotomy sites. In dark grey, the new (already discretized) design domain is shown which retains the symmetry of the facial contour. **(c)** shows the discretized domain in Figure **(b)** again with its voxelized representation with a voxel size of $3\,\mathrm{mm}$ from which the RBF's will be spanned.

design domain constrains volume from being added outside the jawline. On the upper section of Ω, no replacement of the coronoid process on the right side was added, leaving more space to the boundaries of the original mandible. This was done to prevent possible wound dehiscence inside the oral cavity, which has been reported to be a risk in mandibular reconstruction plates [80]. The result of the design process to form the design domain can also be seen in Figure 2.27b. Note that for the sake of simplicity, no connecting flanges were added to Ω. The result is that a perfect bond is assumed between Ω and the remaining mandible. The three resulting geometries were then exported to Gmsh [35] and discretized into a mesh consisting of three parts: the computational domain Ω and the right and left sides of the remaining mandible. These three domains were then discretized in $30\,025$, $16\,804$ and $110\,930$ tetrahedral elements, respectively.

However, the shape and size of the elements in this mesh vary to make the mesh conform to the shape of each domain. As discussed before, the nodes in such a mesh are not suitable as a basis for RBFs from which to span the LSF. The solution is using a voxelized representation, which is depicted in Figure 2.27c. This voxelized mesh with a voxel size of $3\,\mathrm{mm}$ is used as the new basis for the RBFs. It consists of 1256 nodes and thus as many design variables are used to represent the topology of the design in the following optimizations. This voxel size and subsequent number of design variables were chosen to obtain a similar number of FE mesh elements per design variable as the problem in Figure 2.18.

2.2.3. Applied forces on the mandible

With the mandible and Ω discretized, boundary conditions need to be applied to the model. However, unlike most engineering problems, there is uncertainty in these boundary conditions. Since these consist of muscle forces and reaction forces, they can vary significantly between patients depending on, for example, sex, body weight, and clenching task [30, 27, 87]. To account for these variations and make the reconstruction plate truly patient-specific, careful deliberation should be made before deciding which forces should be applied.

In total, 13 muscles are attached to an intact mandible [128]. Of these muscles, 6 are considered principal muscles, namely the superficial masseter (SM), the deep masseter (DM), medial ptygeroid (MP), anterior temporalis (AT), middle temporalis (MT), and posterior temporalis (PT) [87], the attachment points of which are depicted in Figure 2.28. Each of these muscles can apply different forces, depending on the clenching task. The most dominant of these tasks are incisal clenching (INC), left or right unilateral molar clenching (MOL), and left or right group function clenching (GF) [87, 64]. In addition to these muscles, the condylar heads and teeth also apply reaction forces on the mandible during clenching tasks to achieve static equilibrium. The condylar heads oppose all translational movement and the teeth apply vertical reaction force while clenching.

Although TO can be conducted for structures that are subject to multiple load cases, left unilateral molar clenching (LMOL) was chosen as the only applied clenching task in this work for the sake of simplicity. This combination of muscle forces was chosen since it has been reported to result in the largest reaction forces on the teeth [87, 48]. This suggests that this task will also yield the highest stresses in the mandible and will thus be the most critical of the dominant clenching tasks. The net muscle forces that correspond to left molar clenching are shown in Table 2.1. However, to make RP truly patient-specific, these forces should be replaced by values that follow from measurements conducted on the actual patient.

With the set of applied forces known, the net reaction forces of both condyles and the teeth can be calculated. After solving for static equilibrium in the whole mandible, the net force of the left and right condyles are found to

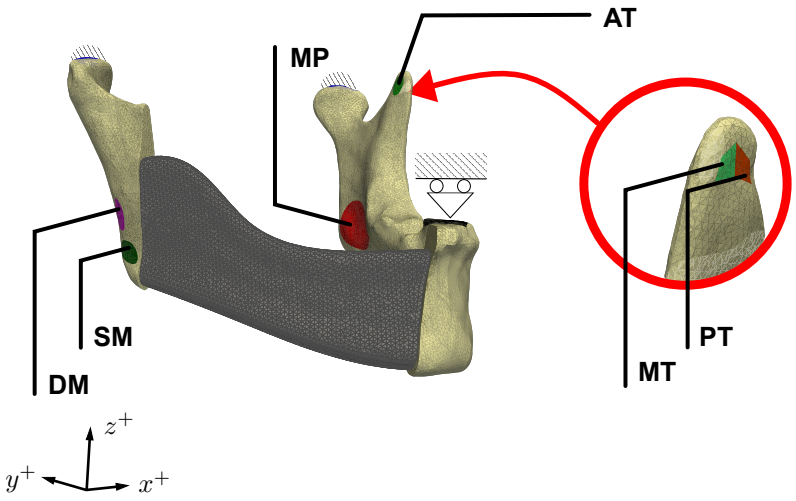

Figure 2.28: The discretizations of Ω and the mandible, combined with a representation of all the attachment points of muscles that are used to apply a force in this work. Note that the mandible is fixed at the condyles and a reaction force in the z-direction is applied to the teeth.

	Right			Left		
	x	y	z	x	y	z
SM	-16.99	-34.49	72.72	20.45	-41.33	87.26
DM	-19.22	12.60	26.71	23.11	15.12	32.04
MP	36.72	-28.15	59.76	-51.41	-39.46	83.59
AT				12.38	-3.67	82.08
MT				10.08	22.68	38.02
PT				6.70	27.43	15.19

Table 2.1: Muscular forces in N in each direction corresponding to the axes in Figure 2.28, according to the left molar clenching task from [87].

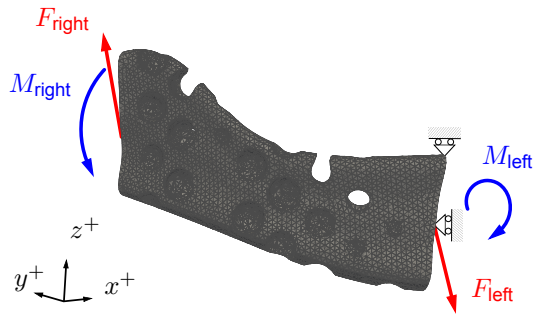

(a)

	LMOL		
	x	y	z
F_{right}	-14.25	7.94	55.70
F_{left}	14.25	-7.94	-55.70
M_{right}	-3.95	-0.86	-0.02
M_{left}	0.59	-1.13	-0.55

(b)

Figure 2.29: The forces that are applied to Ω. **(a)** shows the initial design of the reconstruction plate. The arrows depict the equivalent forces and moments that are applied on the osteotomy sites. **(b)** states the magnitudes of the internal forces in N and moments in $\mathrm{N\,m}$ in each direction that are stated in **(a)**.

be $\begin{bmatrix}-7.06 & 11.29 & -169.35\end{bmatrix}$ N and $\begin{bmatrix}-14.76 & 57.98 & -103.49\end{bmatrix}$ N, respectively. Meanwhile, the vertical reaction force of the teeth that are used during the LMOL clenching task is -224.54 N. Note that, for this specific mandible, the coronoid process on the right side could not be retained during the resection. This means that on this side, the three temporalis muscles also had to be resected and will not apply a force on the mandible. Thus, the corresponding entries in Table 2.1 are empty. A similar approach could be required for the masseter muscles on the right side. Sometimes, the attachment points of these muscles need to be relocated to place the RP or be resected altogether [38]. The required approach depends on the location of the osteotomy sites. However, for this work, it was assumed that the masseter muscles remain intact.

2.2.4. Boundary conditions on the domain

To increase computational efficiency, the domains that represent the remaining parts of the mandible will not be analyzed during the optimization. To still yield the correct boundary conditions on Ω, the applied muscle and reaction forces on each side of the mandible were projected onto the two osteotomy sites. The result of this approach is the internal forces and moments that act on the osteotomy sites. A schematic representation of this situation can be seen in Figure 2.29a. The moments in this load case are applied uniformly about the centroid of both osteotomy sites while the forces are applied uniformly over the same surfaces. This application of loads happens in the form of a Neumann boundary condition on the nodes that lie on the osteotomy site so that the net forces and moments will be equivalent to the internal forces and moments in the osteotomy sites.

In Table 2.29b, these internal forces and moments are stated. Logically, the forces on the left and right cancel each other out in order to retain a static equilibrium of the domain. However, because of the bent shape of Ω, the magnitudes and directions of the moments vary significantly between both sides of the domain. This means that these applied forces and moments will be very specific to the location and size of the defect in the mandible and thus specific to each patient. In the case shown in Figure 2.27b, on the right, the moment works mostly in bending. Meanwhile, on the other side, the applied moment is smaller in magnitude and applies torsion on Ω. This difference in applied load would be expected to influence the shape of the reconstruction plate in later optimized designs and thus will be used to check whether optimized designs are logical or not.

Finally, to prevent solid body rotations and translations of Ω, extra boundary conditions should be applied. Because of its proximity to the teeth, the top of the left osteotomy site of the domain is fixed in the z-direction. However, a fixation in the other directions was not placed here, since the applied moments are expected to be at a maximum this far from the centroid. Thus, at the centroid of this face, the movement in x and y-direction was set to zero using a Dirichlet boundary condition. Of course, this method of preventing solid body translations is incorrect, since the fixed locations would move when the RP is attached to the mandible. However, since fixation flanges were omitted, these boundary conditions were considered adequate for the purposes of this work. With this addition, the whole set of boundary conditions is complete, as visualized in Figure 2.29a. In the same figure, the initial design of the reconstruction plate is also depicted. It consists of a grid of spherical holes, similar to the initial design in Figure 2.18. However, because of the irregular shape of Ω, the ordered grid of holes does not appear as ordered.

2.2.5. Optimized designs of a solid titanium reconstruction plate

With all information on the elastostatic problem of the mandible known, the optimization scheme can finally be applied to the design of a patient-specific mandibular reconstruction plate. The material properties that were assigned to the elements in Ω_s are a Young's modulus $E_s = 116\,\mathrm{GPa}$ and Poisson's ratio $\nu_s = 0.34$, corresponding to the values of titanium in literature [73]. The elements in the void domain Ω_v have a Young's modulus $E_v = 10^{-6}$ and a Poisson's ratio $\nu_v = 0.3$.

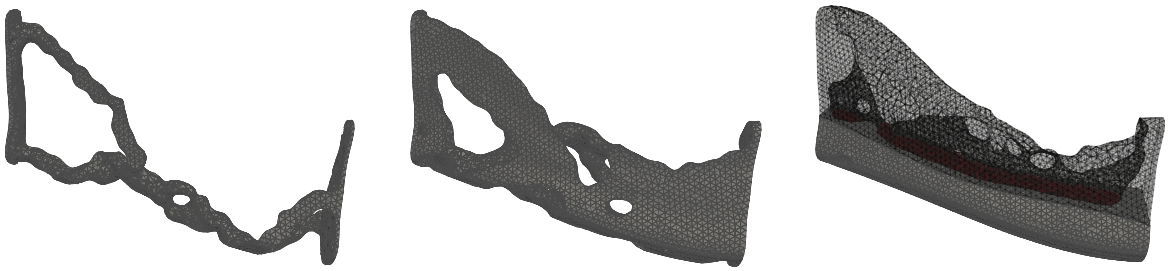

(a) (b) (c)

Figure 2.30: Optimized designs of the mandibular reconstruction plate after 150 iterations if it were to be made from solid titanium. **(a)** shows the optimized design for a maximum volume fraction of $10\,\%$. **(b)** depicts the optimized design that is allowed to use $30\,\%$ of Ω. Note a similar structure on the left of the figure compared to **(a)**, although also more material is distributed towards the right as well to resist torsion. **(c)** shows the final design for optimization with the volume constrained to $50\,\%$ of the design domain. However, this design does not show a lot of detail, since it is made hollow. This is shown by making part of the design transparent. The elements in red are part of the void domain.

As a move limit for the MMA, a value of 0.0002 was set. As before, the LSF was regularized using reinitialization every 15^{th} iteration of the optimization process and the quadratic method was used to place enriched nodes. Also, the optimization was terminated after 150 iterations. The maximum volume of the plate was set to $10\,\%$, $30\,\%$ and $50\,\%$ of Ω, which means the optimization problem was solved three times. The final designs of these three problems can be seen in Figure 2.30.

In Figure 2.30a, where the maximum allowed volume is $10\,\%$ of Ω, the design is very slender. On the left of the figure, where the reconstruction plate connects to the right of the mandible, it is clear that the structure is optimized for a bending load since a triangular structure is formed. However, on the other side of the domain, the design looks illogical. Only two elements are connected to the left osteotomy site, while this section of the design would be expected to be under a torsion-dominated load. Upon further investigation, the cause of this incorrect design is the use of an insufficient number of design variables. Since the design variables are spaced in a voxelized grid, each nearest neighbour of any RBF centre is $3\,\mathrm{mm}$ away. This distance, combined with the radius of each RBF that has a smoothening effect on the LSF, results in a minimal thickness of features. However, when the maximum volume of the design is only allowed to be a small portion of Ω, this minimal feature thickness is problematic since it forces the MMA to reduce the number of strut-like elements in the design. This is visible in Figure 2.30a and can only be solved by reducing the space between the RBFs and thus increasing the number of design variables.

In contrast to the design that only displaces $10\,\%$ of Ω, the design in Figure 2.30b shows a structure that would be expected as a result to the boundary conditions that were applied according to Section 2.2.4. On the side near the right osteotomy site, the design forms a structure that resembles a triangle, which looks similar in shape to the structure in Figure 2.30a. However, on the other side of the design, the structure is more logical than the design with the lowest allowed volume. This design consists of two vertical sections that are parallel to each other, in order to maximize resistance to torsion. In the middle of the optimized design in Figure 2.30b, the design still appears to be bending-dominated. This is expected since M_{right}, which is mainly a bending moment, is larger in magnitude than M_{left}, which is a torsion-dominant moment.

The designs discussed up to this point have a smooth surface, which follows from the formulation of the LSF that is spanned by the RBFs. Also, there is no sign of zigzagging of the material interface, since that is solved by applying a quadratic approximation to the location of enriched nodes. The optimized design that is allowed to use $50\,\%$ of Ω, depicted in Figure 2.30c, appears to fill the entire domain. Upon further investigation, this only appears to be the case, since the final design is mostly hollow. In essence, it consists of two vertical members that are connected at some places in the middle. This can be seen by making the design semi-transparent.

The convergence behaviour of the objective function and the volume constraint related to the designs in Figure 2.30 can be seen in Figure 2.31. The volume constraints behave as expected, with the fraction that is V_s/V_Ω converging smoothly to the prescribed value. After this value has been reached, the volume fraction remains at this value during the rest of the optimization process. The behaviour of the objective function tells a different story, however. For the problem with a maximum volume fraction of $10\,\%$, a lot of oscillations occur during the optimization process. This is also caused by the restriction in the minimum feature thickness that was discussed before. For the domain Ω and its voxelized representation in Figure 2.27c, the RBFs clearly have problems in representing a design that displaced less than $30\,\%$ of Ω. This is the case, as the objective function already starts oscillating when the volume fraction gets below this point. This further supports the assumption that the final design in Figure 2.30a is not

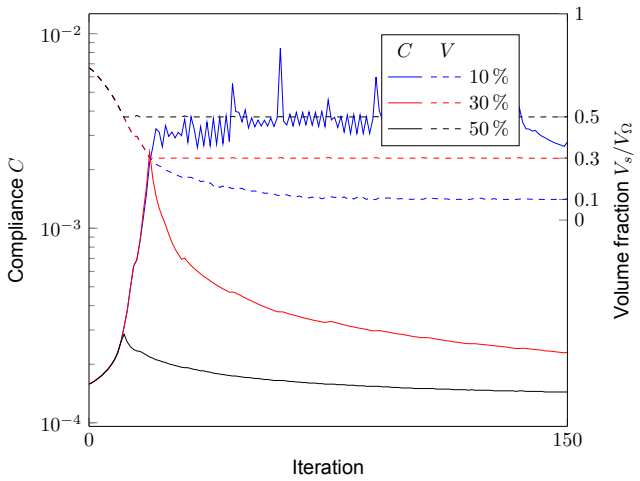

Figure 2.31: The convergence behaviour of the problem of the mandibular reconstruction plate. Note that the behaviour of the compliance C of the design with the smallest allowed volume fraction shows undesired oscillations. The two optimizations with a higher maximum allowed volume on the other hand, show a smooth convergence.

viable. However, the other designs do show a smooth converging behaviour of the objective, suggesting that these designs are indeed viable and the compliance of these structures has successfully been minimized.

2.3. Application of functionally graded materials

2.3.1. The best choice of a functionally graded material

Now that there are optimized designs for a mandibular reconstruction plate, these geometries could be used as a guide for designing the actual reconstruction plate. This is possible since the material near the resection sites gives a good indication of the locations where fixation flanges and screws are required. Moreover, the resulting geometries give an indication of the dominant types of load in each region of the plate. However, the final designs in Figure 2.30 were optimized with the sole objective of minimizing compliance by using solid titanium. This means that the designs presented up to this point will not have any possible means of reducing the risk of stress shielding in the bone surrounding the reconstruction plate. Thus, the focus shifts to improve on the results that were found up to now. To reduce the discrepancy between the stiffness of the bone and that of the reconstruction plate, a functionally graded material could be of use for this objective [59, 111]. To obtain a variation in the material properties depending on the location of Ω, the choice of microstructure to achieve this is very important. There is a range of types of microstructures, each having numerous advantages and disadvantages [46, 50].

One option is to use lattice structures, which have been used to design mandibular reconstruction plates [72, 33, 88]. In these structures, the strut diameters were optimized to, for example, homogenize stresses in the reconstruction plate. However, this does not allow for control over the macroscopic topology of the plate. Foam-like structures can also be used [5, 99], but these lack fine control over material properties throughout the design domain. Moreover, this type of microstructure is irregular and thus the structural integrity of the design cannot be accurately predicted using FEM.

A third option is the use of periodically repeating cells that, contrary to lattice structures, do not consist of struts. The most commonly used of these are Triply Periodic Minimal Surfaces (TPMS). These types of microstructures can be found in nature, for example, butterfly wings and beetle shells [59, 54]. These porous structures have several favourable properties that could be useful in mandibular reconstruction plates. One such property is the possibility to combine a low stiffness with a high fatigue strength. This means the stiffness can be adapted to approach that of trabecular bone while still retaining structural integrity [10, 43]. Also, research shows that the porosity of these structures allows them to be sufficiently permeable, which allows oxygen and nutrients to travel to cells growing in the microstructure [10]. This will aid the healing of the tissue around the plate and promote bone ingrowth. Another advantage is the mean curvature of the pores in the structures, which is approximately zero. This value is comparable to that of trabecular bone, which has also been described to promote bone ingrowth [101, 52]. Because of these advantages, TPMS microstructures have widely been used in the field of tissue engineering [22, 25, 57].

There are many different types of TPMS structures, of which the most common are primitive, diamond, and gyroid [110], each of which have distinct mechanical properties. Research has shown that the gyroid structure shows favourable properties concerning its strength-to-weight ratio [71], while crucially showing good control over its stiff-

ness by changing porosity [127, 126]. Moreover, this type of microstructure also showed favourable bone ingrowth compared to other TPMS structures [77].

The overall size of each unit cell of the microstructure is also very important. This is not only determined by the requirements of the human body but also by the capabilities of the SLM 3D printers that will manufacture the reconstruction plate. This technical constraint is set by the average size of the Ti6Al4V powder particles of which the plate will be produced, which leads to every powder layer having a thickness of at least $50\,\mu\mathrm{m}$ [116, 16]. Each unit cell of the TPMS microstructure must be accurately manufactured, which means that features should be sufficiently larger than this layer thickness. Also, the pore size of the microstructure should have a specific size to provide optimal conditions for bone ingrowth. *In vitro* and *in vivo* experiments have shown that a pore size of approximately $300\,\mu\mathrm{m}$ are optimal for this purpose [116, 10, 55, 89], which gives an even bigger lower bound to the size scale of the microstructure. The use of unit cells with a size of $1.5\,\mathrm{mm}$ x $1.5\,\mathrm{mm}$ x $1.5\,\mathrm{mm}$ has already been shown to exhibit favourable conditions for bone ingrowth in reconstruction plates [10]. This makes the use of gyroid TPMS unit cells with the same size a good choice of microstructure in this work.

However, using one type of microstructure would mean that the material has the same, more flexible, properties throughout the whole domain. Although this could reduce the discrepancy between the stiffness of the reconstruction plate and the bone in the mandible, it would not result in an optimal design. In the middle of the domain, where there is no bone in the proximity, the benefits of a porous microstructure would not outweigh those of a solid material. The increased strength of solid material would allow for a more slender cross-section of the reconstruction plate in this region, reducing the risk of wound dehiscence.

To combine the desired effects of a compliant microstructure in the proximity of the remaining mandible and the stiffness of solid titanium in the middle of the reconstruction plate, a function is constructed that represents this. This function describes the desired Young's modulus throughout the design domain as

$$E(\boldsymbol{x}) = E_0 + \alpha \, \min(|\boldsymbol{x} - \boldsymbol{x}_{\text{ref}}|) \, . \tag{2.32}$$

This equation describes an increasing Young's modulus when moving away from $\boldsymbol{x}_{\text{ref}}$, which can be any set of reference geometries. At the location of these reference geometries, Young's modulus is set to the value of E_0, while α represents the gradient in the elastic modulus with respect to the distance to $\boldsymbol{x}_{\text{ref}}$. In the case of a mandibular reconstruction plate, $\boldsymbol{x}_{\text{ref}}$ contains the two osteotomy sites. To find a material microstructure that follows the desired behaviour that is described by Equation (2.32), another design problem needs to be solved. The Young's modulus that is prescribed can be achieved by changing, for example, the thickness of the membrane in the unit cells [22]. There has been some work on obtaining the required geometrical properties to obtain the desired mechanical properties [69, 70].

2.3.2. Analytical sensitivities of a functionally graded material

Because of this variation of the microstructure, the material constitutive matrix will also vary through every element in the mesh. This variation will need to be taken into account when computing sensitivities. However, in Equation (2.21), $\boldsymbol{D}$ was assumed to be constant in the derivative of the integration element's stiffness matrix with respect to the location of enriched node $\boldsymbol{x}_n$. In the case of a functionally graded material, $\boldsymbol{D}$ is differentiable with respect to the location of enriched node $\boldsymbol{x}_n$:

$$\frac{\partial \boldsymbol{k}_e}{\partial \boldsymbol{x}_n} = \int_{\triangle} \left(\frac{\partial j_e}{\partial \boldsymbol{x}_n} \boldsymbol{B}^{\intercal} \boldsymbol{D} \boldsymbol{B} + j_e \frac{\partial \mathbf{B}^{\intercal}}{\partial \boldsymbol{x}_n} \boldsymbol{D} \boldsymbol{B} + j_e \boldsymbol{B}^{\intercal} \frac{\partial \boldsymbol{D}}{\partial \boldsymbol{x}_n} \boldsymbol{B} + j_e \boldsymbol{B}^{\intercal} \boldsymbol{D} \frac{\partial \boldsymbol{B}}{\partial \boldsymbol{x_n}} \right) \mathrm{d}\boldsymbol{\xi} \, . \tag{2.33}$$

In this equation, the third term, $j_e \boldsymbol{B}^{\intercal} (\partial \boldsymbol{D} / \partial \boldsymbol{x}_n) \boldsymbol{B}$, is new as compared to Equation (2.21). This extra term describes the change in the integration element's material constitutive matrix with respect to the enriched node placement. This can be visualized by looking at an element that is crossed by Γ_m, as depicted in Figure 2.32. It shows that a movement of the interface results in movement of integration points. This in turn changes $\boldsymbol{D}$, which should be taken into account in design sensitivities.

The field that represents the Young's modulus in the elements is described by interpolating the Young's modulus E_i at the parent element's nodes using the parent shape functions N, i.e., $E = \sum_i N_i E_i = \boldsymbol{N} \boldsymbol{E}$. When enriched node $\boldsymbol{x}_n$ is moved towards node 1, as visualized in Figure 2.32, the shapes of integration elements in the support of $\boldsymbol{x}_n$ are changed. This influences the previously mentioned interpolation since the values of the parent element's shape functions at the integration points are dependent on the location of enriched node $\boldsymbol{x}_n$. This can be written down as the following chain rule of derivatives:

$$\frac{\partial \boldsymbol{D}}{\partial \boldsymbol{x}_n} = \frac{\partial \boldsymbol{D}}{\partial E} \frac{\partial (\boldsymbol{N} \cdot \boldsymbol{E})}{\partial \boldsymbol{x}_n} \, . \tag{2.34}$$

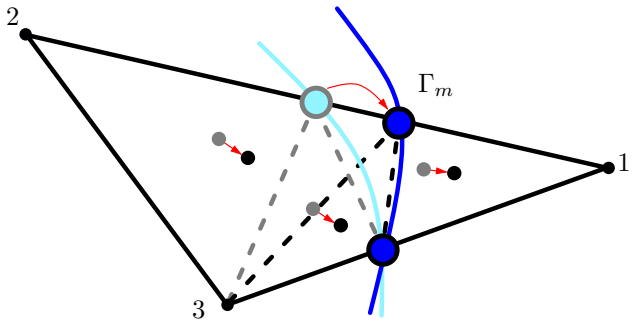

Figure 2.32: An element that is crossed by material interface Γ_m, which is moved from the light blue to the dark blue configuration. This movement changes the shape of the integration elements, which in turn moves the integration points of the integration elements. At these points, the material constitutive matrix is evaluated, which will as a result also change when using a functionally graded material.

The nodal Young's moduli $\boldsymbol{E}$ are defined for the nodes of the parent element and independent of $\boldsymbol{x}_n$, which means that $\partial \boldsymbol{E}/\partial \boldsymbol{x}_n$ is zero. This in turn means that only the derivative of values of the parent element's shape functions at the integration points with respect to the enriched node location is nonzero, which was defined in [13] as

$$\frac{\partial \boldsymbol{N}}{\partial \boldsymbol{x}_n} = \frac{\partial \boldsymbol{N}}{\partial \boldsymbol{\xi}_p} \boldsymbol{A}^{-1} \frac{\partial \boldsymbol{x}_e}{\partial \boldsymbol{x}_n} \boldsymbol{N}_e \,. \tag{2.35}$$

In this equation, $\boldsymbol{A}$ is the isoparametric mapping matrix and $\boldsymbol{\xi}_p$ is the location of the integration point in the parent reference coordinate system. Finally, $\boldsymbol{N}_e$ are the linear Lagrange shape functions associated with the nodes of the integration element, and $\boldsymbol{x}_e$ are the global coordinates of the integration element's nodes.

Following this, the correct implementation of this addition to the derivative of the integration element's stiffness matrix with respect to the location of enriched nodes must be proven. To do this, the analytically computed sensitivities $\partial C/\partial s_i$ were compared to central finite differences C_i' for the same problem shown in Figure 2.9. The circular inclusions in the initial design again have a Young's Modulus $E_v = 1 \times 10^{-6}$. Contrary to before, the material in Ω_s shows the behaviour described by Equation (2.32). The only reference geometry is the right plane, where $E_0 = 1$. Moreover, $\alpha = 99$, which means the Young's modulus will be equal to 100 on the left side of the domain. As before, Poisson's ratio is equal to 0.3 for elements in both Ω_v and Ω_s.

The relative differences of the nonzero design variable sensitivities follow from the same definition as Equation (2.31) and the resulting values of the relative differences δ_i are plotted for a range of finite step sizes Δs_i. Figure 2.33b shows that δ_i converges to zero for a range of step sizes, even for a domain that is made from a functionally graded material. As a reference, Figure 2.33a depicts the relative differences while using the definition of $\partial \boldsymbol{k}_e/\partial \boldsymbol{x}_n$ from Equation (2.21). These values of δ_i are off by large values, which means they appear constant for varying step sizes. This proves the importance of the additional term in $\partial \boldsymbol{k}_e/\partial \boldsymbol{x}_n$ which accounts for the variation in the material constitutive matrix and its correct implementation. Thus the IGFEM method used for level set-based TO in this work can indeed be applied to materials with varying material properties through Ω.

2.3.3. Optimizing the MBB beam problem with a functionally graded material

In order to investigate the influence of a functionally graded material, the MBB beam problem illustrated in Figure 2.5 was revisited. However, this time the material in Ω_s was assigned a Young's modulus according to Equation (2.32) with $E_0 = 1$. This is the case for nodes on the right of the domain. When moving to the left from this reference geometry the material becomes less compliant. The circular inclusions in the initial design again have Young's modulus $E_v = 1 \times 10^{-6}$ and Poisson's ratio of 0.3. As before, an RBF was placed at every FE mesh node, with each of these RBFs having a support radius of $r_s = \sqrt{2}a$. The move limit for the MMA again was set at 0.001, with the optimization being terminated after 100 iterations.

The final designs of these problems for a varying value of α are shown in Figure 2.34. Note that, as a reference, the top design in this figure uses $\alpha = 0$, which is identical to the design in Figure 2.15 with a reinitialization interval of 15 iterations. When comparing this design with designs for which $\alpha \neq 0$, one can see the difference in allocation of the material through Ω. When α is increased, material is moved towards the right of Ω, thickening the struts in this region while making the structure thinner on the left side. Moreover, in the design for which $\alpha = 1$, the third from the top in Figure 2.34, extra strut-like elements are added to the right of the domain. These results agree with what was expected with the addition of functionally graded materials. Thus this approach can be used in more complex problems, such as a mandibular reconstruction plate.

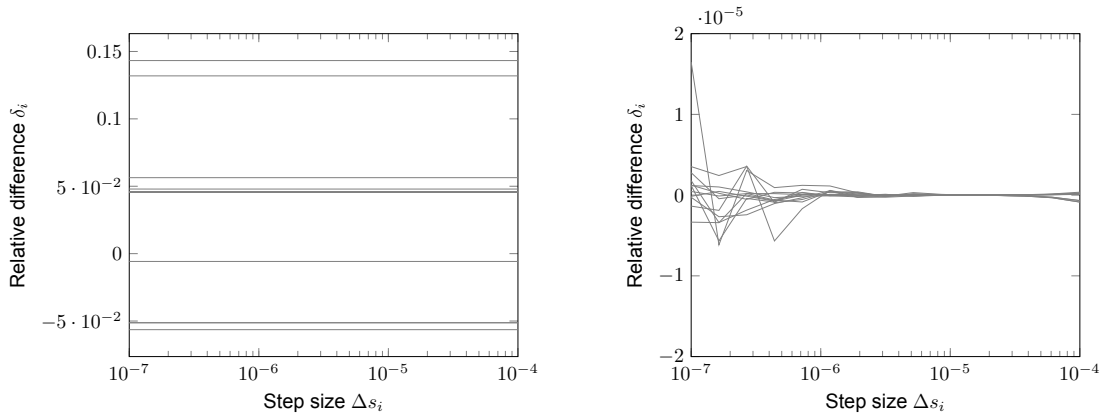

Figure 2.33: Relative differences δ_i as a function of the step size Δs_i for the numerically computed central finite differences C_i'. while using a functionally graded material in Ω_s. The Young's modulus follows the behaviour described in Equation (2.32). **(a)** shows the relative differences when using the derivative of the integration element's stiffness matrix with respect to the enriched node placement from Equation (2.21). This approach results in incorrect analytical sensitivities, which would result in incorrect design updates. **(b)** depicts the same relative differences with the improved definition in Equation (2.33), which shows a range of step sizes for which δ_i converges to zero

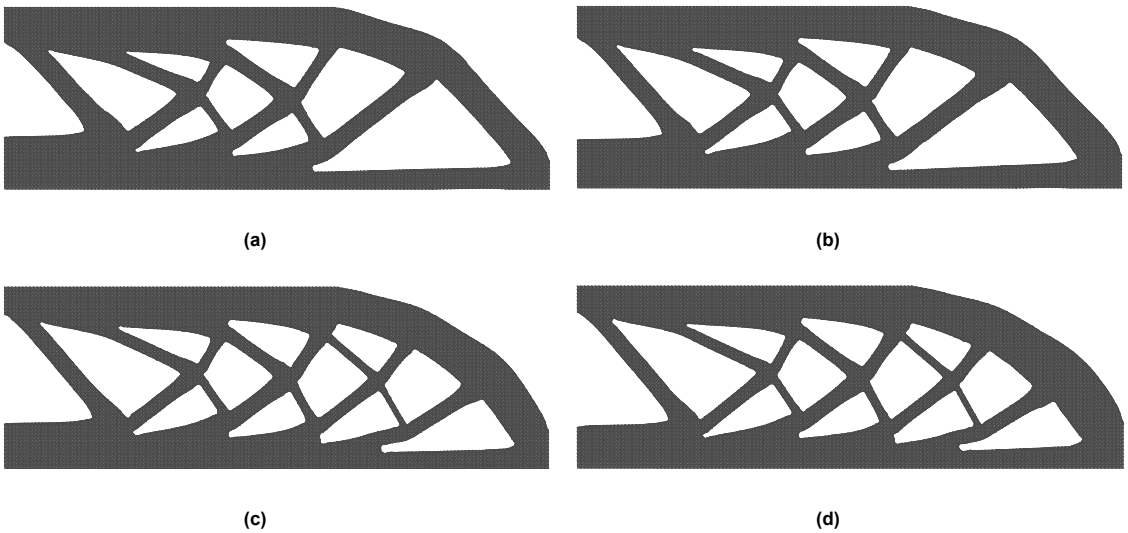

Figure 2.34: Optimized designs while using a functionally graded material according to Equation (2.32). For all designs, $\boldsymbol{x}_{\text{ref}}$ is the right of Ω, at which $E_0 = 1$. **(a)** shows the design when $\alpha = 0$, thus the design is the same as shown in Figure 2.15c. **(b)** displays the final design for $\alpha = 1/3$, which means that the Young's modulus is 2 at the left of the domain. The design is very similar to **(a)**. **(c)** depicts the optimized design for $\alpha = 1$, where extra struts are used to reinforce the right of the domain. **(c)** shows the final design when $\alpha = 3$, so that the Young's modulus is 10 on the left of Ω. One can see the distribution of extra area towards the right side of the domain, where the prescribed Young's modulus indicates a more porous and compliant microstructure.

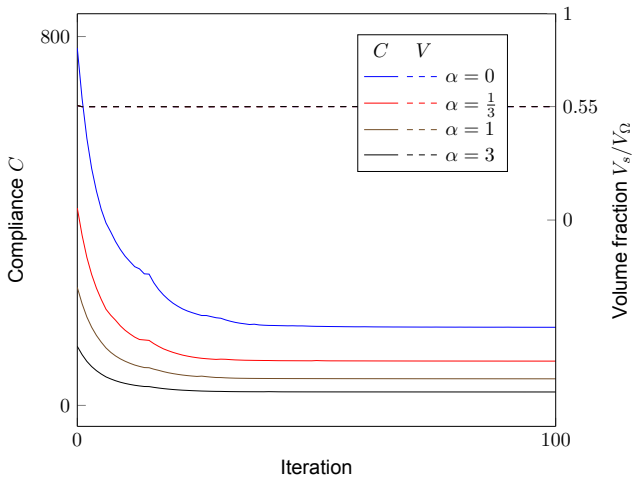

Figure 2.35: The convergence behaviour of both the compliance objective and volume constraint of the MBB beam problem, while using functionally graded materials with different values of α. Note that the final compliance decreases for an increasing value of α.

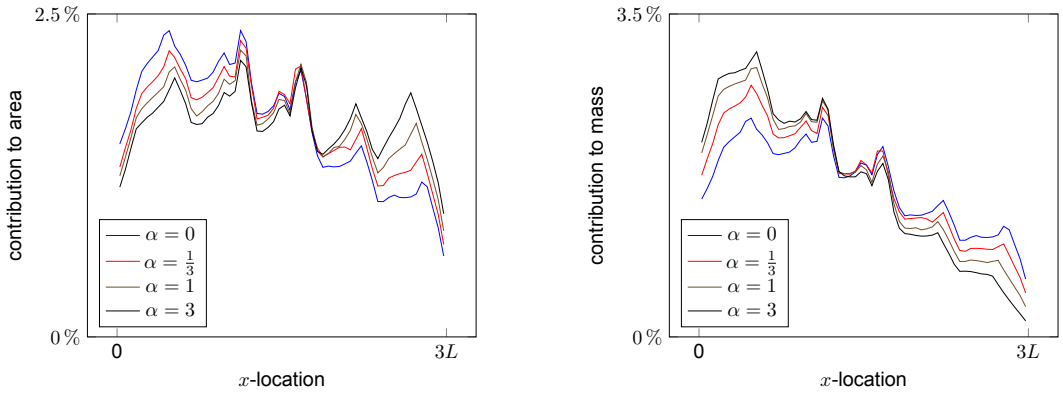

(a) **(b)**

Figure 2.36: Visualizations of material distribution along the x-direction of the MBB beam for the designs in Figure 2.34. **(a)** shows the distribution of area for every design, not accounting for microstructure porosity. The increased area on the right shows that parts with a weaker microstructure are reinforced. **(b)** depicts the mass distribution in the designs in Figure 2.34. Contrary to Figure **(a)**, microstructure porosity is taken into account. This shows that even though the designs appear to reinforce the right of the domain, material is actually moved towards the left, since the microstructure in that location is significantly less porous when using an FGM.

The convergence behaviour of the objective and volume fraction V_s/V_Ω is shown in Figure 2.35. The convergence of the compliance objective shows a logical behaviour. Since an increased value of α leads to an increase in the overall stiffness of the beam, the compliance should be lower when using the functionally graded material used in this problem. This behaviour indeed is visible, while no difference is discernible on the convergence behaviour of the volume fraction.

For more insight into the influence of a gradient in Young's modulus through the domain, Figure 2.36a shows the distribution of area in the design as a function of the x-coordinate. By plotting this for every design in Figure 2.34, a clear comparison can be made between final designs with different values of α. The result clearly shows that for the case of $\alpha = 0$, the majority of the area in the design is distributed towards the left of the domain. When increasing α, this distribution changes and an increasing amount of area is moved towards the right of the domain, where the Young's modulus is the lowest. However, when taking the porous microstructure into account the result is very different. This is depicted in Figure 2.36b and shows that mass is actually moved towards the left when increasing α. To achieve a microstructure is $1/10$ of that of a solid material, the porosity of a typical TPMS microstructure should be $90\,\%$ [120]. This relationship between porosity between porosity and Young's modulus is linear and it heavily influences the results shown in Figure 2.36.

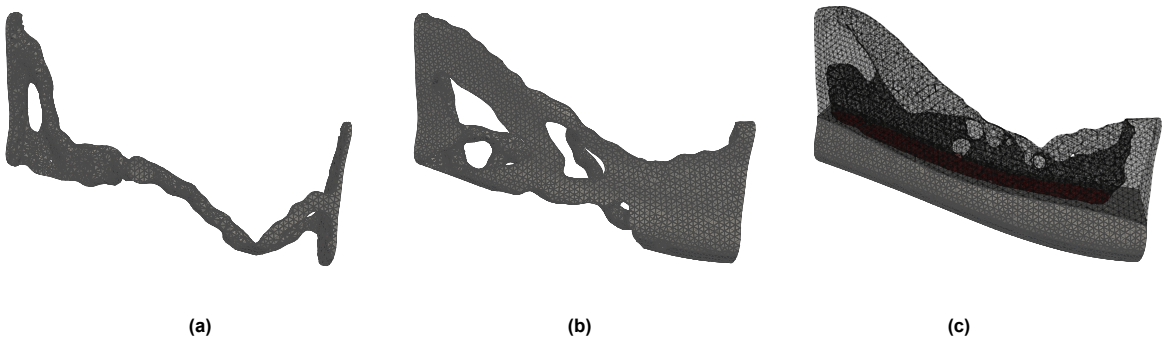

(a) (b) (c)

Figure 2.37: Optimized designs of the mandibular reconstruction plate made out of a functionally graded material after 150 iterations. **(a)** shows the optimized design for a maximum volume fraction of $10\,\%$. Note the changed shape of the elements that are attached to the right osteotomy site. Material was moved to reinforce sections with a more flexible microstructure, thus flattening the triangular structure in Figure 2.30a. **(b)** depicts the optimized design that is allowed to take up $30\,\%$ of Ω. This design also shows material being moved from the middle towards the sides of the reconstruction plate. **(c)** shows the final design for an optimization with a volume constrained to $50\,\%$ of the design domain. However, as before with the same volume fraction, this design does not show a lot of detail, since it is made hollow. This is again shown by making part of the design transparent, showing a cross section with the red void domain.

2.3.4. Optimized designs of a functionally graded reconstruction plate

With functionally graded materials correctly implemented, the same problems that were solved in Section 2.2.5 were optimized. However, the material properties assigned to the elements in Ω_s are now different. Namely, a varying Young's modulus is used that follows the behaviour described in Equation (2.32), where $E_0 = 14\,\mathrm{GPa}$. This is the Young's modulus that is used in the design at both osteotomy sites. It is very compliant compared to the value of $116\,\mathrm{GPa}$ that was used in the designs shown in Figure 2.30 and possible thanks to the use of a microstructure with an estimated porosity of $86\,\%$. In the middle of Ω, however, the desired value of Young's modulus is equal to $116\,\mathrm{GPa}$, corresponding to solid titanium. To achieve this, α was set to $102 \times 10^9\,\mathrm{Pa}/38.86 \times 10^{-3}\,\mathrm{m} = 2.62\,\mathrm{GPa/mm}$, where the denominator is the maximum distance from any node in the mesh to the two reference geometries, which is $38.86\,\mathrm{mm}$. As before, Poisson's ratio $\nu_s = 0.34$, corresponding to titanium. The material properties of elements in the void domain are the same as before.

As stated in Section 2.2.5, the move limit of the MMA was set to 0.0002 and three optimizations were done for the maximum allowed volume fractions of $10\,\%$, $30\,\%$ and $50\,\%$ of Ω. Also, regularization of the LSF occurred every 15^{th} iteration using reinitialization. The optimizations were again terminated after 150 iterations, and the resulting geometries can be seen in Figure 2.37. The optimized design with the lowest volume fraction of $10\,\%$ in Figure 2.37a shows a similar problem to its counterpart in Section 2.2.5. This design is mostly reduced to one beam that connects the two osteotomy sites; the cause of this suboptimal design is again an insufficient number of design variables, which limits the minimal size of features in the design. However, because of the variable microstructure that reduces stiffness in the proximity of bone, the design is different from the one depicted in Figure 2.30a. The optimized design has more material in the regions with the more compliant microstructure. The most material is added on the osteotomy site on the right. On this side, one can also note the disappearance of the triangular structure that could be seen before. In Figure 2.37a, this feature that resulted from the bending moment that is applied is drastically changed in shape in order to stiffen the more compliant microstructure near the osteotomy site.

The optimized design in Figure 2.37b paints a similar picture, although again with a more realistic design thanks to the increased volume that the design is allowed to occupy. This design shows a heavy correlation with the design that was optimized under the assumption that solid titanium would be used. On the left of this figure, the triangular structure that was shown in Figure 2.30b can be seen again. However, this time the lower part of this section is reinforced by an additional structure. All this comes at the cost of more slender struts in the middle of the reconstruction plate. On the right of the figure, not much difference can be seen, since the structure is again mostly hollow in order to resist the applied torsion. The same can be said about the final design of the optimization problem where $50\,\%$ of Ω is allowed to be used. Since this design in Figure 2.37c again appears to entirely fill Ω, not much can be seen in this figure. However, by making part of the design semi-transparent, it can be seen that the design is indeed mostly hollow.

When analyzing the convergence behaviour of the compliance and volume fraction of the three optimization problems, shown in Figure 2.38, one can again see the problem that a low maximum allowed volume fraction poses. This constraint is smoothly approached and maintained during the later parts of the optimization. However, as a result, the compliance of the structure that is only allowed to occupy $10\,\%$ of Ω fluctuates significantly and reaches

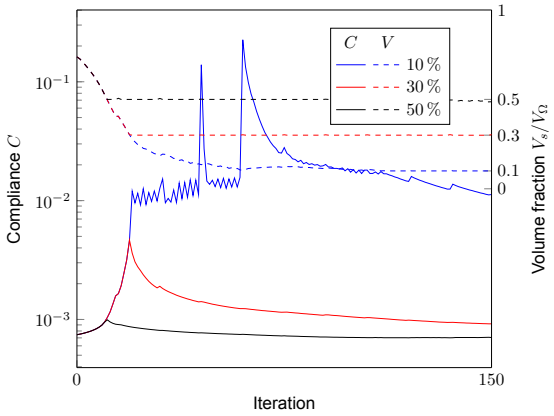

Figure 2.38: The convergence behaviour of the problem of the mandibular reconstruction plate, while using a functionally graded material. Note that the behaviour of the compliance C of the design with the smallest allowed volume fraction shows undesired oscillations again, just like Figure 2.31. The two optimizations with a higher maximum allowed volume on the other hand show a smooth convergence. However, when using an FGM, the compliance of the final designs is significantly higher.

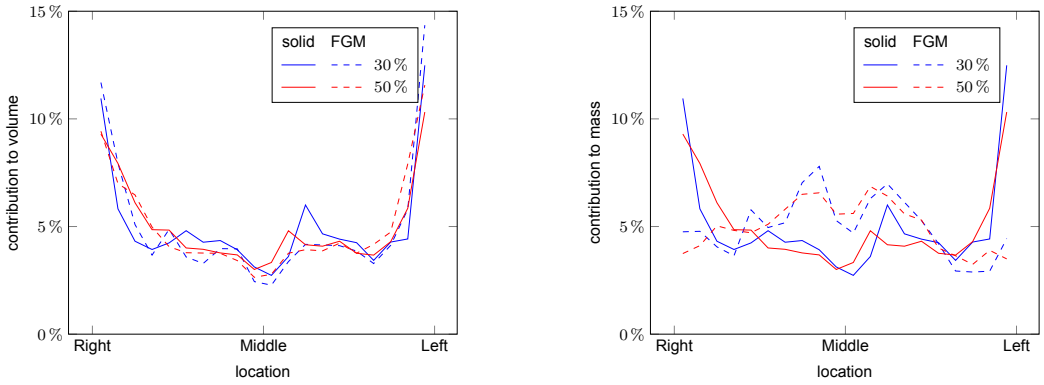

Figure 2.39: Visualizations of material distribution in the optimized designs for the mandibular reconstruction plate beam for the designs in Figures 2.30 and 2.37, divided into 20 sections. For readability, the designs with a maximum volume have been left out. **(a)** shows the distribution of volume for every design, not accounting for microstructure porosity. In this figure, the volume appears to be moved out of the middle towards the sides, where the material Young's modulus is weaker. **(b)** depicts the mass distribution in the designs in Figure 2.34. Contrary to Figure **(a)**, microstructure porosity is taken into account. This again shows that even though material appears to be moved towards the sides in Figure 2.37, because of the high porosity in these regions, material is actually moved towards the middle.

values that could be avoided if more design variables were to be used. The convergence behaviour of the optimizations for the two other maximum allowed volume fractions, however, is as expected. The compliance increases while the volume decreases towards the specified fraction, after which the compliance is minimized while retaining the volume fraction that was set as a constraint. Also, compared to Figure 2.31, the compliance of the designs shown in Figure 2.37 are significantly more compliant.

To analyze the designs more objectively, the material distribution of the designs in Figures2.30 and 2.37 was analyzed. The volume of the elements in each design with a maximum allowed volume fraction of $30\,\%$ and $50\,\%$ is shown in Figure 2.39a. Without accounting for microstructure porosity, it appears that material is distributed towards the osteotomy sites for the designs that use an FGM. This is to reinforce sections where the Young's modulus is prescribed to be lower than in the middle of the plate. This behaviour is similar to that seen in Figure2.36a. But again, the picture changes when the varying microstructure porosity is taken into account. For Figure2.37, solid titanium is used in the middle of the plate and a microstructure with a porosity of $86\,\%$ at both sides. This results in the actual mass being moved towards the middle when using an FGM, as shown in Figure2.39b. Note that the lines in Figure2.39b are the same when using solid titanium, since the porosity is $0\,\%$ through the whole design.

3

Conclusion and recommendations

In some ways, the majority of this work can be seen as a continuation of the work by van den Boom et al. [12] on IGFEM level set-based TO. The zigzagging in the aforementioned work was initially attributed to an approximation error in the deformations and stresses of the structures that were optimized. This work found the underlying cause of this zigzagging of the material interface and proposed a solution in the form of an improved quadratic approximation of the location of enriched nodes along the interface. Moreover, the introduction of a reinitialization scheme of the level set function transforms the problem into one that is more well-posed and less likely to converge to suboptimal local minima. Following these improvements, the topology optimization framework was applied to both two and three-dimensional compliance minimization problems, which indeed showed a smoother and more accurate representation of the inherently smooth zero contour of the level set function spanned by RBFs. Since these improvements focus on the representation of the design, they are not limited to compliance minimization and can be applied to any problem that uses IGFEM level set-based TO.

Moreover, this work also made a starting point on IGFEM level set-based TO on unstructured meshes. This offers an alternative to immersed domains, allowing for more control over the boundaries of the domain. The introduction of a method to voxelize domains of any shape means that the RBFs from which the level set function will be spanned are uniform. By doing this, meshes with local refinements can be used to find more accurate approximations of deformations and stresses in critical regions, such as bearing surfaces and screw holes.

Finally, this work introduced the possibility to perform compliance minimization with IGFEM on structures made out of functionally graded materials. This was done by adding an extra term to the derivative of the stiffness matrix of integration elements with respect to the location of enriched nodes. This approach uses interpolation of the material's Young's modulus using linear shape functions. While it is not implemented in this work, the same approach can be taken in order to account for a variation in Poisson's ratio.

These improvements allow for the application of this structural optimization method on the elastostatic problem of a mandibular reconstruction plate. Moreover, the influence of a functionally graded material was examined to find a way to reduce the risk of stress shielding and subsequent bone resorption. Although a reduction of stress shielding was not proved in this work, the plates using an FGM did show a significantly lower compliance than the designs made out of solid titanium. Also, because of the gradient in the material property in the reconstruction plate, it appeared that more volume was moved towards the osteotomy sites in the optimized designs. However, when accounting for microstructure porosity, it was shown that mass actually moved away from the bone. This means that the functionally graded designs supply substantial porous material near the bone to form a good basis for osseointegration when used *in vivo*.

The regions in which this work has developed new knowledge can also be used as a basis for new research. Below is a summary with just a few alleys in which research could be focused:

- Improvements in the smoothness of the material interface proposed in this work further augment the advantages that IGFEM level set-based TO provides. Thus, the applications that have previously been explored with this technology should be revisited. Examples of these fields are the band gap maximization in the design of phononic crystals [13], the maximization of fracture resistance of structures made out of brittle materials [131] and electromagnetic scattering and eigenvalue problems [7]. The incorrect placement of enriched nodes in these problems influence design updates. Because of this, fluctuations in the objective function can occur which could be solved by the improved approximation of the LSF in this work.

- The introduction of functionally graded materials shows that structures constructed of these types of materials can be optimized with this method. These materials with a gradual change in properties fulfill a desire in a multitude of fields where dissimilar materials need to be connected. One logical field is of course in the field of bone reconstruction, where stress shielding is not just a problem for mandibular reconstruction plates. The same phenomenon has been reported in hip joint replacements, tibial, and dental implants [95, 26, 106]. Another example can be found in the field of thermodynamics, where functionally graded materials fill a critical role in reducing thermal stresses in multi-material structures that are subjected to high temperatures [102]. The definitions established in this work can easily be adapted to optimize heat conductivity issues on materials with varying properties.
- The new possibility of using locally refined meshes in combination with IGFEM level set-based optimization increases the window of possibilities to which this technique can be applied. In the field of mandibular reconstruction plates, the region around screws has been reported to be crucial in terms of stresses [92, 14]. Further research could improve on the optimizations in this work by adding a focus on the flanges with which the reconstruction plate will be fixed to the remaining mandible. By using a refined mesh in the areas in the proximity of these sources of stress concentrations, a more realistic design of a mandibular reconstruction could be obtained.
- The designs in this work focused on achieving a reduction in stress shielding in bone connected to the RP. Although the compliance was shown to be reduced, more work should be put into actually proving a reduction in stress shielding. Multiple metrics in literature have been reported to predict screw loosening, such as the strain energy density transfer parameter (SEDTP) [97, 19] and shear stresses at the bone-implant interface [91, 28]. These metrics should be used to verify later designs that use more realistic means of plate fixation or even as an objective function for optimization problems to more effectively minimize stress shielding.
- This work focused on the optimization of mandibular reconstruction plates that are made of a functionally graded material with decreasing Young's modulus in the vicinity of bone. This could be the starting point of more elaborate research on the influence of the prescribed properties of the material on the optimized design. In this work, solid titanium was only used exactly in the middle of the reconstruction plate, resulting in the lowest spatial gradient in Young's modulus possible for the used domain. However, using a larger region with solid titanium could increase the structural integrity of the design. To the knowledge of the author, no research has been done on the dimensions of the region at which a functionally graded material reduces the effects of stress shielding on bone.

References

[1] Gr Egoire Allaire, Franc ßois Jouve, and Anca-Maria Toader. “Structural optimization using sensitivity analysis and a level-set method q”. In: (). DOI: 10.1016/j.jcp.2003.09.032. URL: www.elsevier.com/locate/jcp.

[2] Samuel Amstutz and Heiko Andrä. “A new algorithm for topology optimization using a level-set method”. In: *Journal of Computational Physics* 216 (2 Aug. 2006), pp. 573–588. ISSN: 0021-9991. DOI: 10.1016/J.JCP.2005.12.015.

[3] Bodard Anne-Gaëlle et al. “Dental implant placement after mandibular reconstruction by microvascular free fibula flap: Current knowledge and remaining questions”. In: *Oral Oncology* 47 (12 Dec. 2011), pp. 1099–1104. ISSN: 13688375. DOI: 10.1016/j.oraloncology.2011.07.016.

[4] James P. Anthony et al. “Donor Leg Morbidity and Function after Fibula Free Flap Mandible Reconstruction”. In: *Plastic and Reconstructive Surgery* 96 (1 July 1995), pp. 146–152. ISSN: 0032-1052. DOI: 10.1097/00006534-199507000-00022.

[5] M. F. Ashby. “The properties of foams and lattices”. In: *Philosophical Transactions of the Royal Society A: Mathematical, Physical and Engineering Sciences* 364 (1838 Nov. 2005), pp. 15–30. ISSN: 1364503X. DOI: 10.1098/RSTA.2005.1678. URL: https://royalsocietypublishing.org/doi/10.1098/rsta.2005.1678.

[6] M. P. Bendsøe. “Optimal shape design as a material distribution problem”. In: *Structural optimization* 1 (4 Dec. 1989), pp. 193–202. ISSN: 09344373. DOI: 10.1007/BF01650949.

[7] Steven van Bergen, Richard A. Norte, and Alejandro M. Aragón. “An interface-enriched generalized finite element method for the analysis and topology optimization of 2-D electromagnetic problems”. In: *Computer Methods in Applied Mechanics and Engineering* 421 (Mar. 2024), p. 116748. ISSN: 00457825. DOI: 10.1016/j.cma.2024.116748.

[8] Reena A. Bhatt and Tamara D. Rozental. “Bone Graft Substitutes”. In: *Hand Clinics* 28 (4 Nov. 2012), pp. 457–468. ISSN: 0749-0712. DOI: 10.1016/J.HCL.2012.08.001.

[9] T. G. BLOCKER and ROY A. STOUT. “MANDIBULAR RECONSTRUCTION, WORLD WAR II”. In: *Plastic and Reconstructive Surgery* 4 (2 Mar. 1949), pp. 153–156. ISSN: 0032-1052. DOI: 10.1097/00006534-194903000-00004.

[10] F. S.L. Bobbert et al. “Additively manufactured metallic porous biomaterials based on minimal surfaces: A unique combination of topological, mechanical, and mass transport properties”. In: *Acta Biomaterialia* 53 (Apr. 2017), pp. 572–584. ISSN: 1742-7061. DOI: 10.1016/J.ACTBIO.2017.02.024.

[11] S ; Van Den Boom et al. “A stable interface-enriched formulation for immersed domains with strong enforcement of essential boundary conditions.” In: *International Journal for Numerical Methods in Engineering Citation* 120 (10 2019), pp. 1163–1183. DOI: 10.1002/nme.6139. URL: https://doi.org/10.1002/nme.6139.

[12] S. J. van den Boom et al. “An interface-enriched generalized finite element method for level set-based topology optimization”. In: *Structural and Multidisciplinary Optimization* 63 (1 2021), pp. 1–20. ISSN: 16151488. DOI: 10.1007/s00158-020-02682-5.

[13] Sanne J. van den Boom et al. “A level set-based interface-enriched topology optimization for the design of phononic crystals with smooth boundaries”. In: *Computer Methods in Applied Mechanics and Engineering* 408 (Apr. 2023). ISSN: 00457825. DOI: 10.1016/J.CMA.2023.115888.

[14] Pter Bujtr et al. “Finite element analysis of the human mandible at 3 different stages of life”. In: *Oral Surgery, Oral Medicine, Oral Pathology, Oral Radiology and Endodontology* 110 (3 2010), pp. 301–309. ISSN: 10792104. DOI: 10.1016/j.tripleo.2010.01.025.

[15] Vivien J. Challis et al. “Prototypes for Bone Implant Scaffolds Designed via Topology Optimization and Manufactured by Solid Freeform Fabrication”. In: *Advanced Engineering Materials* 12 (11 Nov. 2010), pp. 1106–1110. ISSN: 14381656. DOI: 10.1002/adem.201000154.

[16] Kangjie Cheng et al. “A personalized mandibular implant with supporting and porous structures designed with topology optimization – a case study of canine”. In: *Rapid Prototyping Journal* 25 (2 Mar. 2019), pp. 417–426. ISSN: 1355-2546. DOI: 10.1108/RPJ-11-2017-0231. URL: https://www.emerald.com/insight/content/doi/10.1108/RPJ-11-2017-0231/full/html.

[17] Agnieszka Chmielewska and David Dean. “The role of stiffness-matching in avoiding stress shielding-induced bone loss and stress concentration-induced skeletal reconstruction device failure”. In: *Acta Biomaterialia* 173 (Jan. 2024), pp. 51–65. ISSN: 17427061. DOI: 10.1016/j.actbio.2023.11.011.

[18] G Colletti et al. “Technical refinements in mandibular reconstruction with free fibula flaps: outcome-oriented retrospective review of 99 cases.” In: *Acta otorhinolaryngologica Italica : organo ufficiale della Societa italiana di otorinolaringologia e chirurgia cervico-facciale* 34 (5 Oct. 2014), pp. 342–8. ISSN: 1827-675X.

[19] . “Computational simulations of stress shielding and bone resorption around existing and computer-designed orthopaedic screws”. In: *Med. Biol. Eng. Comput* 40 (2002), pp. 311–322.

[20] C Copelli et al. “Management of free flap failure in head and neck surgery.” In: *Acta otorhinolaryngologica Italica : organo ufficiale della Societa italiana di otorinolaringologia e chirurgia cervico-facciale* 37 (5 Oct. 2017), pp. 387–392. ISSN: 1827-675X. DOI: 10.14639/0392-100X-1376.

[21] P.D. Diegel, A.U. Daniels, and H.K. Dunn. “Initial effect of collarless stem stiffness on femoral bone strain”. In: *The Journal of Arthroplasty* 4 (2 Jan. 1989), pp. 173–178. ISSN: 08835403. DOI: 10.1016/S0883-5403(89)80071-3.

[22] Anna Diez-Escudero et al. “Porous polylactic acid scaffolds for bone regeneration: A study of additively manufactured triply periodic minimal surfaces and their osteogenic potential”. In: *Journal of Tissue Engineering* 11 (2020). ISSN: 20417314. DOI: 10.1177/2041731420956541.

[23] N P van Dijk et al. “Level-set methods for structural topology optimization: a review”. In: 48 (2013), pp. 437–472. DOI: 10.1007/s00158-013-0912-y.

[24] N.P. van Dijk, M. Langelaar, and F. van Keulen. “Explicit level□set□based topology optimization using an exact Heaviside function and consistent sensitivity analysis”. In: *International Journal for Numerical Methods in Engineering* 91 (1 July 2012), pp. 67–97. ISSN: 0029-5981. DOI: 10.1002/nme.4258.

[25] Zhifei Dong and Xin Zhao. “Application of TPMS structure in bone regeneration”. In: *Engineered Regeneration* 2 (2021), pp. 154–162. ISSN: 26661381. DOI: 10.1016/j.engreg.2021.09.004.

[26] B. Eidel et al. “Tibial implant fixation in TKA worth a revision?—how to avoid stress-shielding even for stiff metallic implants”. In: *Computer Methods in Biomechanics and Biomedical Engineering* 24 (3 Feb. 2021), pp. 320–332. ISSN: 1025-5842. DOI: 10.1080/10255842.2020.1830274.

[27] T. M.G.J. Van Eijden. “Biomechanics of the Mandible”. In: *http://dx.doi.org/10.1177/10454411000110010101* 11 (1 Jan. 2000), pp. 123–136. ISSN: 10454411. DOI: 10.1177/10454411000110010101. URL: https://journals.sagepub.com/doi/10.1177/10454411000110010101.

[28] Samira Faegh and Sinan Müftü. “Load transfer along the bone–dental implant interface”. In: *Journal of Biomechanics* 43 (9 June 2010), pp. 1761–1770. ISSN: 00219290. DOI: 10.1016/j.jbiomech.2010.02.017.

[29] Bader Fatani, Jumana A Fatani, and Omar A Fatani. “Approach for Mandibular Reconstruction Using Vascularized Free Fibula Flap: A Review of the Literature.” In: *Cureus* 14 (10 Oct. 2022), e30161. ISSN: 2168-8184. DOI: 10.7759/cureus.30161.

[30] V. F. Ferrario et al. “Single tooth bite forces in healthy young adults”. In: *Journal of Oral Rehabilitation* 31 (1 Jan. 2004), pp. 18–22. ISSN: 0305-182X. DOI: 10.1046/j.0305-182X.2003.01179.x.

[31] Jerome H Friedman et al. “An Algorithm fQr Finding Best in Logarithmic Expected Time”. In: *ACYL Transactions on Mathematical Software* 3 (3 1977), pp. 209–226.

[32] Harold M. Frost. “Bone’s Mechanostat: A 2003 Update”. In: *Anatomical Record - Part A Discoveries in Molecular, Cellular, and Evolutionary Biology* 275 (2 2003), pp. 1081–1101. ISSN: 0003276X. DOI: 10.1002/AR.A.10119.

[33] Hui Gao et al. “Mechanobiologically optimization of a 3D titanium-mesh implant for mandibular large defect: A simulated study”. In: *Materials science & engineering. C, Materials for biological applications* 104 (Nov. 2019). ISSN: 1873-0191. DOI: 10.1016/J.MSEC.2019.109934. URL: https://pubmed.ncbi.nlm.nih.gov/31500061/.

[34] A. Gelas et al. “Radial basis functions collocation methods for model based level-set segmentation”. In: *Proceedings - International Conference on Image Processing, ICIP* 2 (2007). ISSN: 15224880. DOI: 10.1109/ICIP.2007.4379136.

[35] Geuzaine, Christophe and Remacle, Jean-Francois. *Gmsh*. Version 4.12.2. Feb. 22, 2023. URL: http://http://gmsh.info/.

[36] Armin Omidvar Ghaziani, Reza Soheilifard, and Sara Kowsar. “The effect of functionally graded materials on bone remodeling around osseointegrated trans-femoral prostheses”. In: *Journal of the Mechanical Behavior of Biomedical Materials* 118 (June 2021), p. 104426. ISSN: 17516161. DOI: 10.1016/j.jmbbm.2021.104426.

[37] Bee Tin Goh et al. *Mandibular reconstruction in adults: a review*. July 2008. DOI: 10.1016/j.ijom.2008.03.002.

[38] Andreas Gravvanis, Dimitrios Anterriotis, and Despoina Kakagia. “Mandibular Condyle Reconstruction With Fibula Free-Tissue Transfer: The Role of the Masseter Muscle”. In: *Journal of Craniofacial Surgery* 28 (8 Nov. 2017), pp. 1955–1959. ISSN: 1049-2275. DOI: 10.1097/SCS.0000000000003998.

[39] Kristina Haase and Gholamreza Rouhi. “Prediction of stress shielding around an orthopedic screw: Using stress and strain energy density as mechanical stimuli”. In: *Computers in Biology and Medicine* 43 (11 Nov. 2013), pp. 1748–1757. ISSN: 00104825. DOI: 10.1016/j.compbiomed.2013.07.032.

[40] R B Haber, C S Jog, and M P Bendsoe. “A new approach to variable-topology shape design using a constraint on perimeter”. In: *Structural Optimization* 11 (1996), pp. 1–12.

[41] Ridha Hambli and Nour Hattab. “Application of Neural Network and Finite Element Method for Multiscale Prediction of Bone Fatigue Crack Growth in Cancellous Bone”. In: *Studies in Mechanobiology, Tissue Engineering and Biomaterials* 14 (2013), pp. 3–30. ISSN: 18682014. DOI: 10.1007/8415_2012_146. URL: https://www.researchgate.net/publication/279272770_Application_of_Neural_Network_and_Finite_Element_Method_for_Multiscale_Prediction_of_Bone_Fatigue_Crack_Growth_in_Cancellous_Bone.

[42] Sandra Hamlet et al. “Mastication and swallowing in patients with postirradiation xerostomia”. In: *International journal of radiation oncology, biology, physics* 37 (4 Mar. 1997), pp. 789–796. ISSN: 0360-3016. DOI: 10.1016/S0360-3016(96)00604-9. URL: https://pubmed.ncbi.nlm.nih.gov/9128953/.

[43] R. Hedayati et al. “How does tissue regeneration influence the mechanical behavior of additively manufactured porous biomaterials?” In: *Journal of the Mechanical Behavior of Biomedical Materials* 65 (Jan. 2017), pp. 831–841. ISSN: 17516161. DOI: 10.1016/j.jmbbm.2016.10.003.

[44] D A Hidalgo. “Fibula free flap: a new method of mandible reconstruction.” In: *Plastic and reconstructive surgery* 84 (1 July 1989), pp. 71–9. ISSN: 0032-1052.

[45] S J Hollister, R D Maddox, and J M Taboas. *Optimal design and fabrication of scaffolds to mimic tissue properties and satisfy biological constraints*. 2002.

[46] Scott J. Hollister. “Porous scaffold design for tissue engineering”. In: *Nature Materials 2005 4:7* 4 (7 2005), pp. 518–524. ISSN: 1476-4660. DOI: 10.1038/nmat1421. URL: https://www.nature.com/articles/nmat1421.

[47] Scott J. Hollister. “Scaffold Design and Manufacturing: From Concept to Clinic”. In: *Advanced Materials* 21 (32-33 Sept. 2009), pp. 3330–3342. ISSN: 1521-4095. DOI: 10.1002/ADMA.200802977. URL: https://onlinelibrary.wiley.com/doi/full/10.1002/adma.200802977%20https://onlinelibrary.wiley.com/doi/abs/10.1002/adma.200802977%20https://onlinelibrary.wiley.com/doi/10.1002/adma.200802977.

[48] Heng Li Huang et al. “Biomechanical analysis of a temporomandibular joint condylar prosthesis during various clenching tasks”. In: *Journal of Cranio-Maxillofacial Surgery* 43 (7 2015), pp. 1194–1201. ISSN: 18784119. DOI: 10.1016/j.jcms.2015.04.016.

[49] R Huiskes, H Weinans, and B van Rietbergen. “The relationship between stress shielding and bone resorption around total hip stems and the effects of flexible materials.” In: *Clinical orthopaedics and related research* (274 Jan. 1992), pp. 124–34. ISSN: 0009-921X.

[50] Dietmar Werner Hutmacher et al. “State of the art and future directions of scaffold-based bone engineering from a biomaterials perspective”. In: *Journal of tissue engineering and regenerative medicine* 1.2 (4 2007), pp. 245–260. ISSN: 1932-6254. DOI: 10.1002/TERM.24. URL: https://pubmed.ncbi.nlm.nih.gov/18038415/.

[51] Jonathan C. Irish et al. “Primary Mandibular Reconstruction with the Titanium Hollow Screw Reconstruction Plate”. In: *Plastic and Reconstructive Surgery* 96 (1 July 1995), pp. 93–99. ISSN: 0032-1052. DOI: 10.1097/00006534-199507000-00014.

[52] H Jinnai et al. “Surface curvatures of trabecular bone microarchitecture”. In: *Bone* 30 (1 Jan. 2002), pp. 191–194. ISSN: 87563282. DOI: 10.1016/S8756-3282(01)00672-X.

[53] P. W. Kämmerer et al. “Local and systemic risk factors influencing the long-term success of angular stable alloplastic reconstruction plates of the mandible”. In: *Journal of Cranio-Maxillofacial Surgery* 42 (5 2014), e271–e276. ISSN: 18784119. DOI: 10.1016/j.jcms.2013.10.004.

[54] Sebastian C. Kapfer et al. “Minimal surface scaffold designs for tissue engineering”. In: *Biomaterials* 32 (29 Oct. 2011), pp. 6875–6882. ISSN: 0142-9612. DOI: 10.1016/J.BIOMATERIALS.2011.06.012.

[55] Vassilis Karageorgiou and David Kaplan. “Porosity of 3D biomaterial scaffolds and osteogenesis”. In: *Biomaterials* 26 (27 Sept. 2005), pp. 5474–5491. ISSN: 0142-9612. DOI: 10.1016/J.BIOMATERIALS.2005.02.002.

[56] Akira Katakura et al. “Material Analysis of AO Plate Fracture Cases”. In: *Oral and Maxillofacial Surgeons J Oral Maxillofac Surg* 62 (2004), pp. 348–352. DOI: 10.1016/j.joms.2003.05.009.

[57] Oraib Al-Ketan, Reza Rowshan, and Rashid K. Abu Al-Rub. “Topology-mechanical property relationship of 3D printed strut, skeletal, and sheet based periodic metallic cellular materials”. In: *Additive Manufacturing* 19 (Jan. 2018), pp. 167–183. ISSN: 22148604. DOI: 10.1016/j.addma.2017.12.006.

[58] Sajad Arabnejad Khanoki and Damiano Pasini. “Multiscale Design and Multiobjective Optimization of Orthopedic Hip Implants with Functionally Graded Cellular Material”. In: *Journal of Biomechanical Engineering* 134 (3 Mar. 2012). ISSN: 0148-0731. DOI: 10.1115/1.4006115.

[59] Nikolaos Kladovasilakis, Konstantinos Tsongas, and Dimitrios Tzetzis. “Finite Element Analysis of Orthopedic Hip Implant with Functionally Graded Bioinspired Lattice Structures”. In: *Biomimetics (Basel, Switzerland)* 5 (3 Sept. 2020). ISSN: 2313-7673. DOI: 10.3390/BIOMIMETICS5030044. URL: https://pubmed.ncbi.nlm.nih.gov/32932596/.

[60] Michael Knitschke et al. “Partial and Total Flap Failure after Fibula Free Flap in Head and Neck Reconstructive Surgery: Retrospective Analysis of 180 Flaps over 19 Years.” In: *Cancers* 13 (4 Feb. 2021). ISSN: 2072-6694. DOI: 10.3390/cancers13040865.

[61] Wayne M. Koch et al. “Advantages of mandibular reconstruction with the titanium hollow screw osseointegrating reconstruction plate (THORP)”. In: *The Laryngoscope* 104 (5 May 1994), pp. 545–552. ISSN: 0023852X. DOI: 10.1002/lary.5541040507.

[62] George Kokosis et al. “Mandibular Reconstruction Using the Free Vascularized Fibula Graft: An Overview of Different Modifications”. In: *Archives of Plastic Surgery* 43 (01 Jan. 2016), pp. 3–9. ISSN: 2234-6163. DOI: 10.5999/aps.2016.43.1.3.

[63] A. van Kootwijk et al. “Semi-automated digital workflow to design and evaluate patient-specific mandibular reconstruction implants”. In: *Journal of the Mechanical Behavior of Biomedical Materials* 132 (2022), p. 105291. ISSN: 1751-6161. DOI: 10.1016/J.JMBBM.2022.105291.

[64] T.W.P. Korioth and A.G. Hannam. “Deformation of the Human Mandible During Simulated Tooth Clenching”. In: *Journal of Dental Research* 73 (1 Jan. 1994), pp. 56–66. ISSN: 0022-0345. DOI: 10.1177/00220345940730010801.

[65] Sebastian Kreissl, Georg Pingen, and Kurt Maute. “An explicit level set approach for generalized shape optimization of fluids with the lattice Boltzmann method”. In: *International Journal for Numerical Methods in Fluids* 65 (5 2011), pp. 496–519. ISSN: 0271-2091. URL: https://www.academia.edu/18930169/An_explicit_level_set_approach_for_generalized_shape_optimization_of_fluids_with_the_lattice_Boltzmann_method.

[66] Batchu Pavan Kumar et al. “Mandibular Reconstruction: Overview”. In: *Journal of Maxillofacial and Oral Surgery* 15 (4 2016), pp. 425–441. ISSN: 0974942X. DOI: 10.1007/s12663-015-0766-5.

[67] Robert Langer and Joseph P. Vacanti. “Tissue engineering”. In: *Science (New York, N.Y.)* 260 (5110 1993), pp. 920–926. ISSN: 0036-8075. DOI: 10.1126/SCIENCE.8493529. URL: https://pubmed.ncbi.nlm.nih.gov/8493529/.

[68] Chia Hsuan Li, Cheng Hsien Wu, and Chun Li Lin. “Design of a patient-specific mandible reconstruction implant with dental prosthesis for metal 3D printing using integrated weighted topology optimization and finite element analysis”. In: *Journal of the Mechanical Behavior of Biomedical Materials* 105 (October 2019 2020), p. 103700. ISSN: 18780180. DOI: 10.1016/j.jmbbm.2020.103700.

[69] Dawei Li et al. “Optimal design and modeling of gyroid-based functionally graded cellular structures for additive manufacturing”. In: *Computer-Aided Design* 104 (Nov. 2018), pp. 87–99. ISSN: 00104485. DOI: 10.1016/j.cad.2018.06.003.

[70] Zhou Li et al. “Performance-based inverse structural design of complex gradient triply periodic minimal surface structures based on a deep learning approach”. In: *Materials Today Communications* 40 (Aug. 2024), p. 109424. ISSN: 23524928. DOI: 10.1016/j.mtcomm.2024.109424.

[71] Fei Liu et al. “Functionally graded porous scaffolds in multiple patterns: New design method, physical and mechanical properties”. In: *Materials & Design* 160 (Dec. 2018), pp. 849–860. ISSN: 02641275. DOI: 10.1016/j.matdes.2018.09.053.

[72] Renshun Liu et al. “Novel Design and Optimization of Porous Titanium Structure for Mandibular Reconstruction”. In: *Applied Bionics and Biomechanics* 2022 (2022). ISSN: 17542103. DOI: 10.1155/2022/8686670.

[73] Yun-Feng Liu et al. “A customized fixation plate with novel structure designed by topological optimization for mandibular angle fracture based on finite element analysis BioMedical Engineering OnLine”. In: *BioMedical Engineering OnLine* 16 (2017), p. 131. DOI: 10.1186/s12938-017-0422-z.

[74] Z Liu, · J G Korvink, and · R Huang. “Struct Multidisc Optim (2005) 29: 407-417 Structure topology optimization: fully coupled level set method via FEMLAB”. In: (). DOI: 10.1007/s00158-004-0503-z. URL: http://www.mscsoftware.com/.

[75] Marc Long and H.J Rack. “Titanium alloys in total joint replacement—a materials science perspective”. In: *Biomaterials* 19 (18 Sept. 1998), pp. 1621–1639. ISSN: 01429612. DOI: 10.1016/S0142-9612(97)00146-4.

[76] Junzhao Luo et al. “A new level set method for systematic design of hinge-free compliant mechanisms”. In: *Computer Methods in Applied Mechanics and Engineering* 198 (2 Dec. 2008), pp. 318–331. ISSN: 0045-7825. DOI: 10.1016/J.CMA.2008.08.003.

[77] Ekaterina Maevskaia et al. “Triply Periodic Minimal Surface-Based Scaffolds for Bone Tissue Engineering: A Mechanical, In Vitro and In Vivo Study”. In: *Tissue Engineering Part A* 29 (19-20 Oct. 2023), pp. 507–517. ISSN: 1937-3341. DOI: 10.1089/ten.tea.2023.0033.

[78] Martta Martola et al. “Fracture of titanium plates used for mandibular reconstruction following ablative tumor surgery”. In: *Journal of Biomedical Materials Research - Part B Applied Biomaterials* 80 (2 2007), pp. 345–352. ISSN: 15524973. DOI: 10.1002/jbm.b.30603.

[79] Peter Maurer et al. “Scope and limitations of methods of mandibular reconstruction: a long-term follow-up”. In: *British Journal of Oral and Maxillofacial Surgery* 48 (2 2010), pp. 100–104. ISSN: 0266-4356. DOI: 10.1016/J.BJOMS.2009.07.005.

[80] Bram B.J. Merema et al. “Novel finite element-based plate design for bridging mandibular defects: Reducing mechanical failure”. In: *Oral Diseases* 26 (6 2020), pp. 1265–1274. ISSN: 1601-0825. DOI: 10.1111/ODI.13331.

[81] Bram Barteld Jan Merema et al. “Patient□specific finite element models of the human mandible: Lack of consensus on current set□ups”. In: *Oral Diseases* 27 (1 2021), p. 42. ISSN: 16010825. DOI: 10.1111/ODI.13381.

[82] M. Mesnard and A. Ramos. “Experimental and numerical predictions of Biomet® alloplastic implant in a cadaveric mandibular ramus”. In: *Journal of Cranio-Maxillofacial Surgery* 44 (5 2016), pp. 608–615. ISSN: 18784119. DOI: 10.1016/j.jcms.2016.02.004.

[83] H. Miura et al. “Chewing ability and quality of life among the elderly residing in a rural community in Japan”. In: *Journal of Oral Rehabilitation* 27 (8 Aug. 2000), pp. 731–734. ISSN: 0305-182X. DOI: 10.1046/j.1365-2842.2000.00590.x.

[84] Papa Ibrahima N’Gom and Alain Woda. “Influence of impaired mastication on nutrition”. In: *The Journal of Prosthetic Dentistry* 87 (6 June 2002), pp. 667–673. ISSN: 00223913. DOI: 10.1067/mpr.2002.123229.

[85] T. Nagasao et al. “Finite element analysis of the stresses around endosseous implants in various reconstructed mandibular models”. In: *Journal of Cranio-Maxillofacial Surgery* 30 (3 2002), pp. 170–177. ISSN: 10105182. DOI: 10.1054/jcms.2002.0310.

[86] Nathaniel Narra et al. “Finite element analysis of customized reconstruction plates for mandibular continuity defect therapy”. In: *Journal of Biomechanics* 47 (1 2014), pp. 264–268. ISSN: 00219290. DOI: 10.1016/j.jbiomech.2013.11.016.

[87] Si Myung Park, Jung Woo Lee, and Gunwoo Noh. “Which plate results in better stability after segmental mandibular resection and fibula free flap reconstruction? Biomechanical analysis”. In: *Oral Surgery, Oral Medicine, Oral Pathology and Oral Radiology* 126 (5 2018), pp. 380–389. ISSN: 22124403. DOI: 10.1016/j.oooo.2018.05.048.

[88] Wen ming Peng et al. “Biomechanical and Mechanostat analysis of a titanium layered porous implant for mandibular reconstruction: The effect of the topology optimization design”. In: *Materials science & engineering. C, Materials for biological applications* 124 (May 2021). ISSN: 1873-0191. DOI: 10.1016/J.MSEC.2021.112056. URL: https://pubmed.ncbi.nlm.nih.gov/33947550/.

[89] Roman A. Perez and Gemma Mestres. “Role of pore size and morphology in musculo-skeletal tissue regeneration”. In: *Materials Science and Engineering: C* 61 (Apr. 2016), pp. 922–939. ISSN: 09284931. DOI: 10.1016/j.msec.2015.12.087.

[90] Dalia Radwan and Fahmy Mobarak. “Plate-related complications after mandibular reconstruction: observational study osteotomy”. In: *Egyptian Journal of Oral and Maxillofacial Surgery* 9 (1 2018), pp. 22–27. ISSN: 2090-097X. DOI: 10.21608/OMX.2018.5623.

[91] Maria Letizia Raffa et al. “Stress shielding at the bone□implant interface: Influence of surface roughness and of the bone□implant contact ratio”. In: *Journal of Orthopaedic Research* 39 (6 June 2021), pp. 1174–1183. ISSN: 0736-0266. DOI: 10.1002/jor.24840.

[92] A. Ramos, R. J. Duarte, and M. Mesnard. “Prediction at long-term condyle screw fixation of temporomandibular joint implant: A numerical study”. In: *Journal of Cranio-Maxillofacial Surgery* 43 (4 2015), pp. 469–474. ISSN: 18784119. DOI: 10.1016/j.jcms.2015.02.013.

[93] A. Ramos, Yi Nyashin, and M. Mesnard. “Influences of geometrical and mechanical properties of bone tissues in mandible behaviour–experimental and numerical predictions”. In: *Computer Methods in Biomechanics and Biomedical Engineering* 20 (9 2017), pp. 1004–1014. ISSN: 14768259. DOI: 10.1080/10255842.2017.1322072.

[94] Ant Onio Ramos et al. “Ex-vivo and in vitro validation of an innovative mandibular condyle implant concept”. In: (2018). DOI: 10.1016/j.jcms.2018.11.010.

[95] M.I.Z. Ridzwan et al. “Problem of Stress Shielding and Improvement to the Hip Implant Designs: A Review”. In: *Journal of Medical Sciences* 7 (3 Mar. 2007), pp. 460–467. ISSN: 16824474. DOI: 10.3923/jms.2007.460.467.

[96] L. Rossetti et al. “The microstructure and micromechanics of the tendon–bone insertion”. In: *Nature Materials 2017 16:6* 16 (6 Feb. 2017), pp. 664–670. ISSN: 1476-4660. DOI: 10.1038/nmat4863. URL: https://www.nature.com/articles/nmat4863.

[97] Gholamreza Rouhi et al. “Prediction of Stress Shielding Around Orthopedic Screws: Time-Dependent Bone Remodeling Analysis Using Finite Element Approach”. In: *Journal of Medical and Biological Engineering* 35 (4 Aug. 2015), pp. 545–554. ISSN: 1609-0985. DOI: 10.1007/s40846-015-0066-z.

[98] G I N Rozvany et al. “Structural Optimization I”. In: (1989), pp. 47–72.

[99] Ap Rubshtein et al. “Porous material based on spongy titanium granules: Structure, mechanical properties, and osseointegration”. In: (2014). DOI: 10.1016/j.msec.2013.11.020. URL: http://dx.doi.org/10.1016/j.msec.2013.11.020.

[100] M.J. de Ruiter and F. van Keulen. “Topology Optimization: Approaching the Material Distribution Problem using a Topological Function Description”. In: pp. 111–119. DOI: 10.4203/ccp.67.1.13.

[101] Monika Rumpler et al. “The effect of geometry on three-dimensional tissue growth”. In: *Journal of The Royal Society Interface* 5 (27 Oct. 2008), pp. 1173–1180. ISSN: 1742-5689. DOI: 10.1098/rsif.2008.0064.

[102] Bassiouny Saleh et al. “30 Years of functionally graded materials: An overview of manufacturing methods, Applications and Future Challenges”. In: *Composites Part B: Engineering* 201 (Nov. 2020), p. 108376. ISSN: 13598368. DOI: 10.1016/j.compositesb.2020.108376.

[103] Harald Schöning and Rüdiger Emshoff. “Primary temporary AO plate reconstruction of the mandible”. In: *Oral surgery, oral medicine, oral pathology, oral radiology, and endodontics* 86 (6 1998), pp. 667–672. ISSN: 1079-2104. DOI: 10.1016/S1079-2104(98)90201-3. URL: https://pubmed.ncbi.nlm.nih.gov/9868722/.

[104] J A Sethian. “Evolution, Implementation, and Application of Level Set and Fast Marching Methods for Advancing Fronts”. In: *Journal of Computational Physics* 169 (2001), pp. 503–555. DOI: 10.1006/jcph.2000.6657.

[105] Takahiko Shibahara et al. “Fracture of Mandibular Reconstruction Plates Used After Tumor Resection”. In: *Oral and Maxillofacial Surgeons J Oral Maxillofac Surg* 60 (2002), pp. 182–185. DOI: 10.1053/joms.2002.29817.

[106] H. Asgharzadeh Shirazi, M. R. Ayatollahi, and A. Asnafi. “To reduce the maximum stress and the stress shielding effect around a dental implant–bone interface using radial functionally graded biomaterials”. In: *Computer Methods in Biomechanics and Biomedical Engineering* 20 (7 May 2017), pp. 750–759. ISSN: 1025-5842. DOI: 10.1080/10255842.2017.1299142.

[107] Sunil S Shroff et al. “Versatility of Fibula Free Flap in Reconstruction of Facial Defects: A Center Study”. In: *Journal of Maxillofacial and Oral Surgery* 16 (1 Mar. 2017), pp. 101–107. ISSN: 0972-8279. DOI: 10.1007/s12663-016-0930-6.

[108] Y Sivanagini, Dhanraj Ganapathy, and Ashish R Jain. *Mental health status of the patients underwent with mandibular resection*. 2018.

[109] Soheil Soghrati et al. “An interface-enriched generalized FEM for problems with discontinuous gradient fields”. In: *International Journal for Numerical Methods in Engineering* 89 (8 Feb. 2012), pp. 991–1008. ISSN: 1097-0207. DOI: 10.1002/NME.3273. URL: https://onlinelibrary.wiley.com/doi/full/10.1002/nme.3273%20https://onlinelibrary.wiley.com/doi/abs/10.1002/nme.3273%20https://onlinelibrary.wiley.com/doi/10.1002/nme.3273.

[110] Baris Sokollu, Orhan Gulcan, and Erhan Ilhan Konukseven. “Mechanical properties comparison of strut-based and triply periodic minimal surface lattice structures produced by electron beam melting”. In: *Additive Manufacturing* 60 (Dec. 2022), p. 103199. ISSN: 22148604. DOI: 10.1016/j.addma.2022.103199.

[111] Antonella Sola, Devis Bellucci, and Valeria Cannillo. “Functionally graded materials for orthopedic applications – an update on design and manufacturing”. In: *Biotechnology Advances* 34 (5 Sept. 2016), pp. 504–531. ISSN: 07349750. DOI: 10.1016/j.biotechadv.2015.12.013.

[112] Niclas Strömberg. “A new multi-scale topology optimization framework for optimal combinations of macro-layouts and local gradings of TPMS-based lattice structures”. In: *Mechanics Based Design of Structures and Machines* 52 (1 Jan. 2024), pp. 257–274. ISSN: 1539-7734. DOI: 10.1080/15397734.2022.2107538.

[113] D R Sumner and J O Galante. “Determinants of stress shielding: design versus materials versus interface.” In: *Clinical orthopaedics and related research* (274 Jan. 1992), pp. 202–12. ISSN: 0009-921X. URL: https://www.researchgate.net/publication/21426792_Determinants_of_Stress_Shielding_Design_Versus_Materials_Versus_Interface.

[114] Hyuna Sung et al. “Global Cancer Statistics 2020: GLOBOCAN Estimates of Incidence and Mortality Worldwide for 36 Cancers in 185 Countries”. In: *CA: A Cancer Journal for Clinicians* 71 (3 May 2021), pp. 209–249. ISSN: 0007-9235. DOI: 10.3322/caac.21660.

[115] Krister Svanberg. “The method of moving asymptotes—a new method for structural optimization”. In: *International Journal for Numerical Methods in Engineering* 24 (2 Feb. 1987), pp. 359–373. ISSN: 1097-0207. DOI: 10.1002/NME.1620240207. URL: https://onlinelibrary.wiley.com/doi/full/10.1002/nme.1620240207%20https://onlinelibrary.wiley.com/doi/abs/10.1002/nme.1620240207%20https://onlinelibrary.wiley.com/doi/10.1002/nme.1620240207.

[116] Naoya Taniguchi et al. “Effect of pore size on bone ingrowth into porous titanium implants fabricated by additive manufacturing: An in vivo experiment”. In: *Materials Science and Engineering: C* 59 (Feb. 2016), pp. 690–701. ISSN: 0928-4931. DOI: 10.1016/J.MSEC.2015.10.069.

[117] S Testelin. “[History of microsurgical reconstruction of the mandible].” In: *Annales de chirurgie plastique et esthetique* 37 (3 June 1992), pp. 241–5. ISSN: 0294-1260.

[118] Stavros Thomopoulos et al. “Collagen fiber orientation at the tendon to bone insertion and its influence on stress concentrations”. In: *Journal of Biomechanics* 39 (10 Jan. 2006), pp. 1842–1851. ISSN: 0021-9290. DOI: 10.1016/J.JBIOMECH.2005.05.021.

[119] HK Uhthoff and ZF Jaworski. “Bone loss in response to long-term immobilisation”. In: *The Journal of Bone and Joint Surgery. British volume* 60-B (3 Aug. 1978), pp. 420–429. ISSN: 0301-620X. DOI: 10.1302/0301-620X.60B3.681422.

[120] Dvina Valainis et al. “Integrated additive design and manufacturing approach for the bioengineering of bone scaffolds for favorable mechanical and biological properties”. In: *Biomedical Materials* 14 (6 Sept. 2019), p. 065002. ISSN: 1748-605X. DOI: 10.1088/1748-605X/ab38c6.

[121] Michael Yu Wang, Xiaoming Wang, and Dongming Guo. “A level set method for structural topology optimization”. In: *Computer Methods in Applied Mechanics and Engineering* 192 (1-2 Jan. 2003), pp. 227–246. ISSN: 00457825. DOI: 10.1016/S0045-7825(02)00559-5.

[122] Holger Wendland. “Piecewise polynomial, positive definite and compactly supported radial functions of minimal degree”. In: *Advances in Computational Mathematics* 4 (1 Dec. 1995), pp. 389–396. ISSN: 10197168. DOI: 10.1007/BF02123482/METRICS. URL: https://link.springer.com/article/10.1007/BF02123482.

[123] Frank Wilde et al. “Multicenter study on the use of patient-specific CAD/CAM reconstruction plates for mandibular reconstruction”. In: *International Journal of Computer Assisted Radiology and Surgery* 10 (12 Dec. 2015), pp. 2035–2051. ISSN: 1861-6410. DOI: 10.1007/s11548-015-1193-2.

[124] Dongming Xiao et al. “An integrated approach of topology optimized design and selective laser melting process for titanium implants materials”. In: *Bio-Medical Materials and Engineering* 23 (5 2013), pp. 433–445. ISSN: 09592989. DOI: 10.3233/BME-130765.

[125] Shintaro Yamasaki et al. “A structural optimization method based on the level set method using a new geometry□based re□initialization scheme”. In: *International Journal for Numerical Methods in Engineering* 83 (12 Sept. 2010), pp. 1580–1624. ISSN: 0029-5981. DOI: 10.1002/nme.2874.

[126] Chunze Yan et al. “Advanced lightweight 316L stainless steel cellular lattice structures fabricated via selective laser melting”. In: *Materials & Design* 55 (Mar. 2014), pp. 533–541. ISSN: 02613069. DOI: 10.1016/j.matdes.2013.10.027.

[127] A. Yánez et al. “Gyroid porous titanium structures: A versatile solution to be used as scaffolds in bone defect reconstruction”. In: *Materials & Design* 140 (Feb. 2018), pp. 21–29. ISSN: 02641275. DOI: 10.1016/j.matdes.2017.11.050.

[128] Olivia Yost et al. “Masticatory System: Anatomy and Function”. In: (Mar. 2020). Ed. by Enriqueta C. Bond et al. DOI: 10.17226/25652. URL: https://www.ncbi.nlm.nih.gov/books/NBK557988/.

[129] Amir A. Zadpoor. “Bone tissue regeneration: the role of scaffold geometry”. In: *Biomaterials Science* 3 (2 Jan. 2015), pp. 231–245. ISSN: 2047-4849. DOI: 10.1039/C4BM00291A. URL: https://pubs.rsc.org/en/content/articlehtml/2015/bm/c4bm00291a%20https://pubs.rsc.org/en/content/articlelanding/2015/bm/c4bm00291a.

[130] A. N. Zeller et al. “Patient-Specific Mandibular Reconstruction Plates Increase Accuracy and Long-Term Stability in Immediate Alloplastic Reconstruction of Segmental Mandibular Defects”. In: *Journal of Maxillofacial and Oral Surgery* 19 (4 Dec. 2020), pp. 609–615. ISSN: 0972-8279. DOI: 10.1007/s12663-019-01323-9.

[131] Jian Zhang, Fred van Keulen, and Alejandro M. Aragón. “On tailoring fracture resistance of brittle structures: A level set interface-enriched topology optimization approach”. In: *Computer Methods in Applied Mechanics and Engineering* 388 (Jan. 2022), p. 114189. ISSN: 00457825. DOI: 10.1016/j.cma.2021.114189.

[132] Hongming Zong et al. “VCUT level set method for topology optimization of functionally graded cellular structures”. In: *Computer Methods in Applied Mechanics and Engineering* 354 (Sept. 2019), pp. 487–505. ISSN: 00457825. DOI: 10.1016/j.cma.2019.05.029.

A

Design velocities for quadratic enriched node placement

Assuming that $\phi_k \neq (\phi_i + \phi_j)/2$, which would mean that a linear interpolation should be used, the zeros of this function are

$$\zeta_n = \frac{-\phi_i + \phi_j \pm \sqrt{8\phi_k\left(-\phi_i - \phi_j + 2\phi_k\right) + \left(\phi_i - \phi_j\right)^2}}{2\left(-\phi_i - \phi_j + 2\phi_k\right)} . \tag{A.1}$$

The zero of this function at which an enriched node is placed, is the value of ζ_n that satisfies $-1 \leq \zeta_n \leq 1$. When applying the inverse mapping of $\zeta(\boldsymbol{x})$, the global location of the enriched node is

$$\boldsymbol{x}_n = \boldsymbol{x}_i + \frac{\zeta_n + 1}{2}\left(\boldsymbol{x}_j - \boldsymbol{x}_i\right) . \tag{A.2}$$

The partial derivatives of this definition with respect to ϕ_i, ϕ_j and ϕ_k are:

$$\frac{\partial \zeta_n}{\partial \phi_i} = \frac{1 - \frac{2\phi_i - 2\phi_j - 8\phi_k}{2\sqrt{-2\phi_i\phi_j - 8\phi_i\phi_k + \phi_i^2 - 8\phi_j\phi_k + \phi_j^2 + 16\phi_k^2}}}{2\left(\phi_i + \phi_j - 2\phi_k\right)} - \frac{-\sqrt{-2\phi_i\phi_j - 8\phi_i\phi_k + \phi_i^2 - 8\phi_j\phi_k + \phi_j^2 + 16\phi_k^2} + \phi_i - \phi_j}{2\left(\phi_i + \phi_j - 2\phi_k\right)^2} \tag{A.3}$$

$$\frac{\partial \zeta_n}{\partial \phi_k} = \frac{-\sqrt{-2\phi_i\phi_j - 8\phi_i\phi_k + \phi_i^2 - 8\phi_j\phi_k + \phi_j^2 + 16\phi_k^2} + \phi_i - \phi_j}{\left(\phi_i + \phi_j - 2\phi_k\right)^2} - \frac{-8\phi_i - 8\phi_j + 32\phi_k}{4\left(\phi_i + \phi_j - 2\phi_k\right)\sqrt{-2\phi_i\phi_j - 8\phi_i\phi_k + \phi_i^2 - 8\phi_j\phi_k + \phi_j^2 + 16\phi_k^2}} \tag{A.4}$$

$$\frac{\partial \zeta_n}{\partial \phi_j} = \frac{-\frac{-2\phi_i + 2\phi_j - 8\phi_k}{2\sqrt{-2\phi_i\phi_j - 8\phi_i\phi_k + \phi_i^2 - 8\phi_j\phi_k + \phi_j^2 + 16\phi_k^2}} - 1}{2\left(\phi_i + \phi_j - 2\phi_k\right)} - \frac{-\sqrt{-2\phi_i\phi_j - 8\phi_i\phi_k + \phi_i^2 - 8\phi_j\phi_k + \phi_j^2 + 16\phi_k^2} + \phi_i - \phi_j}{2\left(\phi_i + \phi_j - 2\phi_k\right)^2} \tag{A.5}$$